NASA Contractor Report 179517

3-D INELASTIC ANALYSIS METHODS FOR HOT SECTION COMPONENTS

Third Annual Status Report
For the Period
February 14, 1985 to February 14, 1986

Volume II
Advanced Special Functions Models

R. B. Wilson and P. K. Banerjee

Contract NAS3-23697
August 1987

NASA

1.REPORT NO. NASA CR-179517	2. GOVERNMENT AGENCY	3.RECIPIENT'S CATALOG NO.
4.TITLE AND SUBTITLE 3-D INELASTIC ANALYSIS METHODS FOR HOT SECTION COMPONENTS - Third Annual, Vol. II, Advanced Special Functions Models		5. REPORT DATE August 1987 6. PERFORMING ORG. CODE
7.AUTHOR(S) R. B. Wilson and P. K. Banerjee		8. PERFORMING ORG. REPT. NO. PWA-5940-46
9.PERFORMING ORG. NAME AND ADDRESS UNITED TECHNOLOGIES CORPORATION Pratt & Whitney, Engineering Division 400 Main St., East Hartford, CT 06108		10. WORK UNIT NO. 11. CONTRACT OR GRANT NO. NAS3-23697
12. SPONSORING AGENCY NAME AND ADDRESS National Aeronautics and Space Administration Lewis Research Center Project Manager, C. C. Chamis, MS 49-6 21000 Brookpark Road, Cleveland, OH 44135		13. TYPE REPT./PERIOD COVERED Third Annual Status Report, Volume II 14. SPONSORING AGENCY CODE RTOP 533-04-1A
15. SUPPLEMENTARY NOTES		

16. ABSTRACT

This Annual Status Report presents the results of work performed during the third year of the 3-D Inelastic Analysis Methods for Hot Section Components program (NASA Contract NAS3-23697). The objective of the program is to produce a series of new computer codes that permit more accurate and efficient three-dimensional analyses of selected hot section components, i.e., combustor liners, turbine blades and turbine vanes. The computer codes embody a progression of mathematical models and are streamlined to take advantage of geometrical features, loading conditions, and forms of material response that distinguish each group of selected components. This report is presented in two volumes. Volume I (NASA CR-179494) describes effort performed under Task IVB, "Special Finite Element Special Functions Models," while Volume II concentrates on Task IVC, "Advanced Special Functions Models."

17. KEY WORDS (SUGGESTED BY AUTHOR(S))	18. DISTRIBUTION STATEMENT
3-D Inelastic Analysis, Finite Elements, Boundary Elements, High Temperature, Creep, Vibration, Buckling, Solution Methods, Constitutive Modeling	General Release

19. SECURITY CLASS THIS (REPT)	20. SECURITY CLASS THIS (PAGE)	21. NO. PGS	22. PRICE *
Unclassified	Unclassified	78	

* For sale by the National Technical Information Service, Springfield, VA 22161

PREFACE

This volume of the Annual Status Report describes the results of work performed on the development of the boundary element method during the third year of the NASA Hot Section Technology program, "3-D Inelastic Analysis Methods for Hot Section Components" (contract NAS3-23697). The goal of the program is to develop computer codes which permit more accurate and efficient structural analyses of gas turbine blades, vanes, and combustor liners. The program is being conducted under the direction of Dr. C. C. Chamis of the NASA-Lewis Research Center. Prime contractor activities at United Technologies Corporation are managed by Dr. E. S. Todd. Subcontractor efforts in the development of the boundary element method, at the State University of New York at Buffalo, are led by Professor P. K. Banerjee.

Contents

1. INTRODUCTION 1

2. SUMMARY 3

3. BOUNDARY ELEMENT METHOD 4

3.1 OVERVIEW 4

3.2 LITERATURE SURVEY UPDATE 6

3.3 FORMULATION DEVELOPMENT 7

3.3.1 SUMMARY 7

3.3.2 QUASI-STATIC ANALYSIS 7

3.3.2.1 REVIEW 7

3.3.2.2 VARIABLE STIFFNESS PLASTICITY 8

3.3.2.3 VOLUME INTEGRATION ALGORITHM . . . 11

3.3.2.4 ANISOTROPIC ELASTICITY 13

3.3.2.5 APPLICATION OF PARTICULAR INTEGRALS 19

3.3.2.6 REPRESENTATION OF HOLES/CAVITIES . . 23

3.3.2.7 GENERALIZED FUNCTIONAL REPRESENTATIONS 28

3.3.3 TRANSIENT AND DYNAMIC STRESS ANALYSIS . . 32

3.3.3.1 REVIEW 32

3.3.3.2 FURTHER DEVELOPMENT OF THE ELASTODYNAMIC FORMULATION 33

3.3.3.3 EXTENSION TO NONLINEAR TRANSIENT DYNAMICS 36

3.4 COMPUTER PROGRAM DEVELOPMENT 39

3.4.1 INTRODUCTION 39

3.4.2 GLOBAL PROGRAM STRUCTURE 39

3.4.3 PROGRAM INPUT 41

3.4.4 IMPLEMENTATION OF VARIABLE STIFFNESS PLASTICITY 41

3.4.5 INCORPORATION OF PARTICULAR INTEGRALS . . 43

3.4.6 EXTRACTION OF EIGENVALUES 43

3.4.7 NONLINEAR DYNAMICS 45

3.4.7.1 TIME-STEPPING 46

3.4.7.2 ITERATIVE SOLUTION ALGORITHM FOR DYNAMIC PLASTICITY 47

3.5 VALIDATION/VERIFICATION 49

3.5.1 SUMMARY 49

3.5.2 MULTI-REGION INTERFACES 50

3.5.3 PLASTICITY USING VARIABLE STIFFNESS ALGORITHM 50

3.5.4 THERMAL/INELASTIC ANALYSIS USING PARTICULAR INTEGRALS 52

3.5.5 BAR SUBJECTED TO TRANSIENT END LOAD 56

3.5.6 SPHERICAL CAVITY SUBJECTED TO DYNAMIC PRESSURE 59

3.5.7 DYNAMIC LOADING ON A SQUARE FOOTING ON A HALF SPACE 63

3.5.8 NONLINEAR DYNAMIC RESPONSE OF A BAR 67

3.5.9 NATURAL FREQUENCIES OF A PARALLELEPIPED 68

3.5.10 COMPONENT ANALYSIS 71

3.6 CONCLUSIONS 74
3.7 LIST OF SYMBOLS 75
3.8 REFERENCES 76

List of Figures

3.1 Relationship of Single Crystal Material to Isotropy 16
3.2 Cube Containing a Cavity 26
3.3 Load as a Function of Cavity Size 27
3.4 Effect of Cavity Shape on Load 28
3.5 Accuracy of Response Near Cavity 29
3.6 Geometric Model of Low Cycle Fatigue Specimen 30
3.7 Beam Deflection ($\nu = 0$) 31
3.8 Beam Deflection ($\nu = .35$) 32
3.9 BEST3D - Overall Program Structure 40
3.10 Incorporation of Particular Integrals 44
3.11 Simulated Disk/Attachment BEST3D Model 51
3.12 Stress-Strain Response 51
3.13 Load - Displacement Response 52
3.14 Stress Variation through Thickness of Cylinder 53
3.15 Boundary Element Model of a Thin Disk 54
3.16 Dynamic Stress in Square Cantilever under End Load 56
3.17 Deflection at Free End of Square Cantilever 57
3.18 Surface Discretization of a Circular Bar 58
3.19 Axial Stress at Midspan of Circular Bar 58
3.20 Axial Displacement at Free End of Circular Bar 59

3.21 Deviatoric Stress at the Cavity Surface 60
3.22 Radial Expansion of Cavity under Triangular Pulse 61
3.23 Radial Expansion of Cavity under Rectangular Pulse 62
3.24 Spherical Cavity Engulfed by a Pressure Wave 62
3.25 Mesh Used for the Analysis of Spherical Cavity 63
3.26 Hoop Stress Induced by Passage of Pressure Wave 64
3.27 Radial Displacements Induced by Passage of Pressure Wave 64
3.28 BEST3D Models for Analysis of Footing Compliance 65
3.29 Vertical Compliance of Flexible Square Footing 66
3.30 Transient Response of Flexible Square Footing 68
3.31 Transient Elasto-Plastic Response of a Bar Subjected to a Suddenly Applied and Maintained End Pressure 69
3.32 Geometry for Calibration of BEST3D Natural Frequency Analysis 71
3.33 BEST3D Model of Anisotropic Turbine Blade 72
3.34 BEST3D Model of Single Pitch of Bearing Race 73
3.35 Hoop Stress Contours for Bearing Race 73

List of Tables

3.1 Calibration of Major BEST3D Capabilities 49

3.2 Free Thermal Expansion of a Thin Disk — $(b-a)/t = 20$ 55

3.3 Free Thermal Expansion of a Thin Disk — $(b-a)/t = 100$ 55

3.4 Comparison of Vertical Compliances Obtained Using Two Different Meshes 67

3.5 BEST3D Models for $1 \times 1 \times 0.5$ Parallelepiped 70

3.6 Convergence of BEST3D Natural Frequency Results 70

3.7 Comparison of Ritz and BEST3D Results for Short, Thick Plate 70

1. INTRODUCTION

Aircraft powerplant fuel consumption and expenditures for repair/replacement of worn or damaged parts make up a significant portion of commercial aviation's direct operating costs. For modern gas turbines, both factors depend heavily on the degree to which elevated flowpath temperatures are sustained in the hot section modules of the engine. Higher temperatures reduce fuel consumption by raising the basic efficiency of the gas generator thermodynamic cycle. At the same time, these elevated temperatures work to degrade the durability of structural components (combustor liners, turbine blades and vanes, airseals, etc.) that must function adjacent to or within the hot gaspath itself, leading in turn to larger maintenance/material costs. Pursuit of the best compromise between performance and durability presents a challenge that will continue to tax the ingenuity of advanced gas turbine design analysts for years to come.

Hot section durability problems appear in a variety of forms, ranging from oxidation/corrosion, erosion, and distortion (creep deformations to occurrence of fatigue cracking. Even modest changes in shape, from erosion or distortion of airfoils for example, can lead to measurable performance deterioration that must be accurately predicted during propulsion system design to insure that long-term efficiency guarantees can be met. Larger distortions introduce serious problems such as hot spots and profile shifts resulting from diversion of cooling air, high vibratory stresses associated with loose turbine blade shrouds, difficult disassembly/reassembly of mating parts at overhaul, etc. These problems must be considered and efforts made to eliminate their effects during the engine design/development process. Initiation and propagation of fatigue cracks represents a direct threat to component structural integrity and must be thoroughly understood and accurately predicted to insure continued safe and efficient engine operation.

Accurate prediction of component fatigue lives is strongly dependent on the success with which inelastic stress/strain states in the vicinity of holes, fillets, welds, and other discontinuities can be calculated. Stress/strain computations for hot section components are made particularly difficult by two factors - the high degree of geometrical irregularity which accompanies sophisticated cooling schemes, and complex nonlinear material behavior associated with high temperature creep/plasticity effects. Since cooling air extraction reduces engine cycle efficiency, concerted efforts are made to minimize its use with the result that elaborate internal passages and surface ports are employed to selectively bathe local regions (airfoil leading edges, louver liner lips, etc.) for which the high temperature environment is most severe. These cooling features frequently interrupt load paths and introduce complex temperature gradients to the extent that the basic assumptions of one- and two-dimensional stress analysis procedures are seriously compromised and the use of three-dimensional techniques becomes mandatory. Even in the presence of cooling, component temperature and stress levels remain high relative to the material's melting point

and yield strength values. The combinations of centrifugal, aerodynamic, thermal, and other mechanical loadings that typically occur in flight operation then serve to drive the underlying material response beyond accepted limits for linear elastic behavior and into the regime characterized by inelastic, time-dependent structural deformations. Thus, an ability to account for both complexities, three-dimensional and inelastic effects, becomes essential to the design of durable hot section components.

General purpose finite element computer codes containing a variety of three-dimensional (brick) elements and inelastic material models have been available for more than a decade. Incorporation of such codes into the hot section design process has been severely limited by high costs associated with the extensive labor/computer/time resources required to obtain reasonably detailed results. Geometric modeling systems and automated input/output data processing packages have received first attention from software developers in recent years and will soon mature to the point that previous over-riding manpower concerns will be alleviated. A prohibitive amount of Central Processing Unit (CPU) time is still required for execution of even modest-size three-dimensional inelastic stress analyses, however, and is chief among the obstacles remaining to be remedied. With today's computers and solution algorithms, models described by a few hundred displacement degrees of freedom commonly consume one to three hours of mainframe CPU time during simulation of a single thermomechanical loading cycle. A sequence of many such cycles may, of course, be needed to reach the stabilized conditions of interest. Since accurate idealizations of components with only a few geometrical discontinuities can easily contain several thousand degrees of freedom, inelastic analysis of hot section hardware with existing codes falls outside the realm of practicality.

The Inelastic Methods Program addresses the need to develop more efficient and accurate three-dimensional inelastic structural analysis procedures for gas turbine hot section components. A series of new, increasingly rigorous, stand-alone computer codes is being created for the comprehensive numerical analysis of combustor liners, turbine blades and vanes. Theoretical foundations for the codes feature mechanics of material models, special finite element models, and boundary element models. Heavy attention is being given to evolution of novel modeling methods that permit non-burdensome yet accurate representations of geometrical discontinuities such as cooling holes and coating cracks. A selection of constitutive relations has been provided for economical or sophisticated description of inelastic material behavior, as desired. Finally, advantages which accrue from application of the improved codes to actual components will be demonstrated by execution of benchmark analyses for which experimental data exist.

2. SUMMARY

The 3-D Inelastic Analysis Methods program is divided into two 24-month segments: a base program, and an option program which was exercised in February 1985. During the base program, a series of new computer codes embodying a progression of mathematical models (mechanics of materials, special finite element, boundary element) was developed for the streamlined analysis of combustor liners, turbine blades and turbine vanes. These models address the effects of high temperatures and thermal/mechanical loadings on the local (stress/strain) and global (dynamics, buckling) structural behavior of the three selected components.

The base program (Tasks I and II) dealt with "linear/polynomial" theory in the sense that stresses/strains and temperatures in generic modeling regions are linear/polynomial functions of the spatial coordinates, and solution increments for load, temperature and/or time are extrapolated accordingly from previous information. The computer codes, developed during the base program, hereafter referred to as MOMM (Mechanics of Materials Model), MHOST (MARC-HOST), and BEST3D (Boundary Element Stress Technology Three-Dimensional), are described in the First and Second Annual Status Reports (NASA CR-174700 and NASA CR-175060).

The option program (Tasks IV and V) will extend the models to include higher-order representations of deformations and loads in space and time and deal more effectively with collections of discontinuities such as cooling holes and coating cracks. Work on Task IV has been completed. Continued development of the BEST3D (Boundary Element Stress Technology Three Dimensional) code has constituted a very important accomplishment of the Task IV effort. The basic BEM (Boundary Element Method) algorithms have been extended to allow improved treatment of inhomogeneous elastic material properties, thermal loading and plastic deformation. In addition, the time embedded elastodynamic algorithm has been expanded to account for nonlinear effects. The results of the boundary element method development (Advanced Formulation Development - Task IVC) are given in the subsequent sections of this volume.

3. BOUNDARY ELEMENT METHOD

3.1 OVERVIEW

It is the goal of the advanced formulation development portion of this program to develop a computational technique for the solution of linear, nonlinear and transient problems in gas turbine engine hot section components. This technique is to be distinct from, and complementary to, the Finite Element Method. The existence of such a computational method will enhance the ability to calibrate the other codes developed under this contract. In addition, it is to be expected that different techniques will prove optimal, in terms of efficiency or accuracy, for particular types of component analysis. Since almost all general purpose structural analysis computer programs presently available employ the displacement finite element method, the new program developed as part of the advanced formulation development effort can be expected to extend the ability to perform realistic analyses of hot section components.

During the first year of this program (Task IC), Pratt & Whitney and its subcontractor, the State University of New York at Buffalo (SUNY-B), developed a new general purpose structural analysis program, BEST3D (Boundary Element Stress Technology), based on the use of the Boundary Element Method (BEM). During this work, the boundary element method was implemented for very general three-dimensional geometries, for elastic, inelastic and dynamic stress analysis problems.

In the second year of the program (Task IIC), Pratt & Whitney and SUNY-B continued the theoretical and numerical development and the computer implementation of the BEM, making very significant advances in a variety of areas, including:

- Incorporation of substructuring capability in nonlinear boundary element method stress analysis.
- Algorithm development, coding and validation of an embedded time algorithm for elastodynamic problems.
- Initial development of a method for representing the effects of embedded discontinuities without explicit boundary modeling.
- Verification of the nonlinear solution capabilities of BEST3D using externally generated data.

The development of the boundary element method during the Base Program is discussed in detail in the 1st and 2nd Annual Status Reports (NASA CR-174700 and NASA CR-175060).

During the first year of the Option Program (Task IVC), the analytical basis of the boundary element method has been significantly extended and improved capabilities have been incorporated in BEST3D. In addition various aspects of the formulation development, not yet incorporated in BEST3D, have been tested using a variety of smaller stand-alone codes. In particular significant effort has been devoted to the following:

- Significant improvement of the time embedded elastodynamic analysis, including the incorporation of linear time variation of field quantities.
- The initial development, coding and testing of a boundary element algorithm for time-embedded nonlinear dynamic analysis.
- Significant improvements in the volume integral based plasticity algorithms, including the incorporation of a variable stiffness plasticity algorithm and indirect calculation of the most highly singular volume integral terms.
- Development of a comprehensive formulation for the use of particular integrals to represent body force, inhomogeneity and discontinuity effects.
- Coding and checkout of a (multi-region) BEST3D capability for the determination of natural frequencies and mode shapes.
- Further validation/verification of BEST3D.

The work carried out in these areas as part of Task IVC is discussed in detail in the following sections.

3.2 LITERATURE SURVEY UPDATE

During the last year there have been two major conferences on boundary element methods. One was held in Lake Como, Italy, while the other was a part of the ASME Winter Annual meeting held in Miami. It was interesting to note that although nearly 150 papers were presented in these two conferences, only a few represented a major advance in the state of the art.

Nishimura described an approximate two-dimensional boundary element formulation for the transient coupled problem of flow through a porous medium. Paris and Garrido examined the use of nonconforming elements in two-dimensional multiregion contact problems, in which they considered opening and closing as well as adhesive and frictional slipping and sliding of subregions. Kamiya and Sawaki examined the problem of converting the volume integration into an equivalent surface integral using a polynomial expansion of the body force field together with the divergence theorem. Li and Brebbia examined the use of axisymmetric curvilinear coordinate systems in boundary element analysis in a very general manner. All of these papers were presented in the Lake Como conference.

Ahmad, Banerjee, Wilson, Miller and Snow presented three papers essentially describing developments in inelastic and dynamic analysis as incorporated in BEST3D. Rizzo and Shippy described developments in periodic dynamic analysis, similar to methods incorporated in BEST3D. Mukherjee and Chandra recently presented further developments in large deformation analysis of axisymmetric solids by the boundary element method. Brebbia reported a novel boundary element method formulation for transient and periodic two-dimensional problems using a real variable method which utilizes the fundamental solutions of the static elastic problem. Annigeri, Gerstle and Ingraffea, Polch, *et. al.* examined a variety of problems involving the modeling of crack tip singularities. Kline in an excellent paper examined the use of parallel processing and solution of block banded system equations in a substructured boundary element analysis. All of these papers were presented in the ASME Winter Annual Meeting (Cruse, T. A., A. Pifko and H. Armen, *Advanced Topics in Boundary Element Analysis*, AMD Vol. 72, ASME, N.Y., 1985).

3.3 FORMULATION DEVELOPMENT

3.3.1 SUMMARY

Important advances have been made during Task IVC in extending the BEM formulation for three-dimensional stress analysis of gas turbine engine structures. The most significant advances have been in the areas of dynamic analysis, where an improved linear formulation and an initial nonlinear formulation were developed and implemented, in the exploitation of particular integrals of the equilibrium equations to represent a wide variety of volume based phenomena and in the three-dimensional development of a variable stiffness plasticity algorithm, incorporating the constitutive relationship within the boundary element system matrix. The extended or newly developed formulations are discussed in the subsections below. The basic BEM formulation is only very briefly reviewed, as full details are available in the First and Second Annual Status Reports (NASA CR-174700 and NASA CR-175060).

3.3.2 QUASI-STATIC ANALYSIS

3.3.2.1 REVIEW By making use of the reciprocal work theorem, the governing differential equations for a three-dimensional (homogeneous) structure under combined thermal, mechanical and body force loadings can be converted to an integral equation written on the surface of the structure. This integral equation is:

$$c_{ij}u_i = \int_S (G_{ij}t_i - F_{ij}u_i)\,dS + \int_V (G_{ij}f_i + \beta W_j T)\,dV \tag{3.1}$$

where T = temperature, $W_j = T_{ikj}\delta_{ik}$, β = coefficient of thermal expansion, T_{ikj} = the stress, σ_{ik}, due to a point force system, e_j, and G_{ij}, T_{ikj} and F_{ij} are defined in the First Annual Status Report (NASA CR-174700). The equation

$$\sigma_{ij} = \int_S (D_{ijk}t_k - S_{ijk}u_k)\,dS + \int_V (T_{ijk}t_k + M_{ij}T)\,dV \tag{3.2}$$

allows calculation of stresses at any interior point where they are required. A similar equation for interior displacements can be obtained by setting $c_{ij} = \delta_{ij}$ in (3.1).

In a purely elastic problem BEM stress analysis can be carried out entirely on the boundary of the structure. Once a physically reasonable set of boundary conditions has been prescribed, (3.1) can, in principle, be solved for all of the remaining boundary displacements and tractions.

It is generally impossible to solve (3.1) exactly for real structures and loading conditions. Suitable approximations of the boundary geometry, displacements and tractions must be

used in order to reduce (3.1) to a system of algebraic equations. The present version of BEST3D models boundary geometry and boundary values of field quantities using linear and/or quadratic isoparametric shape functions. The surface integrals in (3.1) are then evaluated numerically using product Gaussian quadrature rules. The numerical implementation of the BEM is discussed in detail in textbooks by Banerjee and Butterfield and by Brebbia, as well as in the First and Second Annual Status Reports (NASA CR-174700 and CR-175060).

In the case of inelastic analysis, the volume integrals in (3.1) cannot be calculated *a priori*, since they require knowledge of inelastic strain, which is itself a part of the solution. In this case equations (3.1), (3.2) and the inelastic material model can be regarded as a coupled system of nonlinear equations. In the numerical implementation of the BEM (3.2) is used to calculate the stresses at interior points, and the nonlinear material model is then used to evaluate inelastic strain. Since the volume integrals of inelastic strain vanish except in regions of nonlinear material response, approximations of geometry and field quantities are required only where nonlinearity is expected. In BEST3D volume models utilize quadratic isoparametric shape functions to model strain variation within volume cells. Three constitutive models are presently included in BEST3D:

1. Von Mises model with isotropic variable hardening
2. Two-surface model for cyclic plasticity
3. Combined plasticity and creep model of Walker.

These constitutive models are discussed in detail in the First and Second Annual Status Reports (NASA CR-174700 and NASA CR-175060).

The remainder of Section 3.3.2 discusses significant new developments carried out during Task IVC.

3.3.2.2 VARIABLE STIFFNESS PLASTICITY A new approach is outlined for BEM formulations for elasto-plasticity, which exploits certain features of the constitutive relationships involved. The unknown nonlinear terms in the interior are now defined as scalar variables. A new direct numerical solution scheme comparable to the variable stiffness method used in finite element analysis has been developed and applied to a number of standard plasticity problems.

For a standard elasto-plastic flow problem the evolution of plastic flow is governed by:

$$F(\sigma_{ij}, h) = 0 \tag{3.3}$$

$$\dot{\epsilon}^{p}_{ij} = \dot{\lambda}\frac{\partial F}{\partial \sigma_{ij}} \tag{3.4}$$

These equations together with the consistency relations (i.e., the stress point must remain on a newly developing yield surface characterized by a change in the hardening parameter h) leads to an expression for the unknown plastic flow factor $\dot{\lambda}$ as:

$$\dot{\lambda} = L^{\sigma}_{ij}\, \dot{\sigma}_{ij} \tag{3.5}$$

where

$$L^{\sigma}_{ij} = \frac{1}{H}\frac{\partial F}{\partial \sigma_{ij}}$$

$$H = -\left(\frac{\partial F}{\partial \epsilon^{p}_{mn}} + \frac{\partial F}{\partial h}\frac{\partial h}{\partial \epsilon^{p}_{mn}}\right)\frac{\partial F}{\partial \sigma_{mn}}$$

It should be noted that L^{σ}_{ij} depends upon the current state variable, not on the incremental quantities.

However, the relationship given by (3.5) does not exist for ideal plasticity, as H vanishes for zero hardening. This can be avoided by reformulating the above expression in terms of strain increments:

$$\dot{\lambda} = L^{\epsilon}_{ij}\dot{\epsilon}_{ij} \tag{3.6}$$

where

$$\begin{aligned} L^{\epsilon}_{ij} &= \frac{1}{H'}\frac{\partial F}{\partial \sigma_{ij}} \\ H' &= \frac{\partial F}{\partial \sigma_{kl}} D_{klmn}\frac{\partial F}{\partial \sigma_{mn}} - \left(\frac{\partial F}{\partial \epsilon^{p}_{kl}} + \frac{\partial F}{\partial h}\frac{\partial F}{\partial \epsilon^{p}_{kl}}\right)\frac{\partial f}{\partial \sigma_{kl}} \end{aligned}$$

where D_{ijkl} is the elastic constitutive tensor. It is evident that H' does not vanish for zero hardening (ideal plasticity).

The basic boundary element formulation for an inelastic body undergoing infinitesimal strain is given by:

$$c_{ij}\dot{u}_i(\xi) = \int_{\Gamma}[G_{ij}(x,\xi)\dot{t}_i(x) - F_{ij}(x,\xi)\dot{u}_i(x)]\, d\Gamma + \int_{\Omega} B_{ijk}(x,\xi)\, \dot{\sigma}^{0}_{ij}\, d\Omega \tag{3.7}$$

The stress rates at an interior point ξ are obtained from equation (3.7) via the strain-displacement relations and the constitutive relationships ($\dot{\sigma}_{ij} = D^{e}_{ijkl}\dot{\epsilon}_{kl} - \dot{\sigma}^{0}_{ij}$) as

$$\begin{aligned} \dot{\sigma}_{ij}(\xi) &= \int_{\Gamma}[G^{\sigma}_{ijk}(x,\xi)\dot{t}_i(x) - F^{\sigma}_{ijk}(x,\xi)\dot{u}_i(x)]\, d\Gamma \\ &\quad + \int_{\Omega} B^{\sigma}_{ipjk}(x,\xi)\, \dot{\sigma}^{0}_{ip}(x)\, d\Omega + J^{\sigma}_{ipjk}\, \dot{\sigma}^{0}_{ip}(\xi) \end{aligned} \tag{3.8}$$

where the kernel functions have been defined in the Second Annual Status Report (NASA CR-175060).

In equation (3.8) the volume integral must be evaluated in the sense of $(\Omega - D)$ with the limit taken as $D \to 0$, where D is a spherical exclusion of small arbitrary radians with ξ as its center. The term J^{σ} is the jump term derived from the analytical treatment of the integral over D. It is of considerable interest to note that the value of J^{σ} is independent of the size of the exclusion D, provided the initial stress distribution is locally homogeneous, i.e. uniform over its volume.

The evaluation of strains and stresses at boundary points can be accomplished by considering the equilibrium of the boundary segment and utilizing constitutive and kinematic equations. The stresses and global derivatives of the displacements which lead to strains at a point ξ can be obtained from the following set of coupled equations:

$$\begin{aligned} \dot{\sigma}_{ij}(\xi) - (\Delta\delta_{ij}\dot{u}_{k,k}(\xi) + \mu(\dot{u}_{i,j}(\xi) + \dot{u}_{j,i}(\xi))) &= -\dot{\sigma}^{0}_{ij}(\xi) \\ \dot{\sigma}_{ij}(\xi)n_j(\xi) &= \dot{t}_i(\xi) \\ \frac{\partial \xi_k}{\partial \eta_l}\frac{\partial \dot{u}_i(\xi)}{\partial \xi_k} &= \frac{\partial \dot{u}_i(\xi)}{\partial \eta_l} \end{aligned} \tag{3.9}$$

where η_i are a set of local axes at the field point ξ.

All the above nonlinear formulations include initial stresses in the governing equations which are not known *a priori* and, therefore, are solved by using iterative procedures. A non-iterative direct solution procedure is made feasible in this work by reducing the number of unknowns in the governing equations by utilizing certain features of the incremental theory of plasticity expressed by equations (3.3) to (3.6). The initial stresses σ^{0}_{ij} appearing in equations (3.7) to (3.9) can be expressed in the context of an elastoplastic deformation as:

$$\dot{\sigma}^{0}_{ij} = K_{ij}\dot{\lambda} \tag{3.10}$$

where $K_{ij} = D^{e}_{ijkl}\dfrac{\partial F}{\partial \sigma_{kl}}$.

Substituting (3.5) and (3.10) in equations (3.7) and (3.8) we can obtain:

$$c_{ij}\dot{u}_i(\xi) = \int_{\Gamma}[G_{ij}(x)\dot{t}_i(x) - F_{ij}(x,\xi)\dot{u}_i(x)]\,d\Gamma \tag{3.11}$$

and

$$\begin{aligned} \dot{\lambda}(\xi) &= L^{\sigma}_{jk}(\xi)\int_{\Gamma}[G^{\sigma}_{ijk}(x,\xi)\dot{t}_i(x) - F^{\sigma}_{ijk}(x,\xi)\dot{u}_i(x)]\,d\Gamma \\ &\quad + L^{\sigma}_{jk}(\xi)\int_{\Omega} B^{\sigma}_{ipjk}(x,\xi)\,K_{ip}(x)\,\dot{\lambda}(x)\,d\Omega \\ &\quad + L^{\sigma}_{jk}\,J^{\sigma}_{ipjk}\,K_{ip}(\xi)\,\dot{\lambda}(\xi) \end{aligned} \tag{3.12}$$

Equations (3.11) and (3.12) can be solved simultaneously to evaluate the unknown values of displacements, traction rates and the scalar variable $\dot{\lambda}$.

The equations for the boundary nodes (3.9) are similarly transformed to express them in terms of the scalar variable $\dot{\lambda}$ using equations (3.5) and (3.10).

3.3.2.3 VOLUME INTEGRATION ALGORITHM Assuming that the boundary and a representative area of the volume (which is likely to yield) is divided into N isoparametric boundary elements and M isoparametric volume cells respectively, we can express the coordinates as well as the displacements, tractions and the scalar flow parameter $\dot{\lambda}$ in terms of their nodal values as:

$$\begin{aligned} x_i &= N^\alpha(\eta)\bar{x}_i^\alpha \\ u_i &= N^\alpha(\eta)\bar{u}_i^\alpha \\ t_i &= N^\alpha(\eta)\bar{t}_i^\alpha \end{aligned}$$

over surface patches, and

$$\begin{aligned} x_i &= M^\beta(\eta)\bar{x}_i^\beta \\ \sigma_{ij}^0 &= M^\beta(\eta)\bar{\sigma}_{ij}^\beta \\ \dot{\lambda}_i &= M^\beta(\eta)K_{ij}\bar{\dot{\lambda}}^\beta \end{aligned}$$

over volume cells, where α and β represent, respectively, the nodal points of boundary elements and volume cells.

The boundary integral equations for displacement (3.11) can then be represented as:

$$\begin{aligned} c_{ij}u_i(x_0^p) = &\sum_{n=1}^{N}\{\int_{\Gamma_n} G_{ij}[x^n(\eta), x_0^p]\; N^\alpha(\eta)\; \bar{t}_i^{\alpha n}\; d\Gamma_n \\ &- \int_{\Gamma_n} F_{ij}[x^n(\eta), x_0^p]\; N^\alpha(\eta)\; \bar{u}_i^{\alpha n}\; d\Gamma_n\} \\ &+ \sum_{m=1}^{M}\int_{\Omega_m} B_{ipj}[x^m(\eta), x_0^p]\; M^\beta(\eta)\; K_{ip}\; \bar{\dot{\lambda}}^{\beta n}\; d\Omega_m \end{aligned} \tag{3.13}$$

The evaluation of the surface integrals involved has been extensively documented in the published literature, notably by Lachat and Watson, who first developed the use of isoparametric surface elements for elastic analysis. A more efficient technique developed in this work has been outlined in the previous annual report (NASA CR-175060).

The volume integral is transformed and the quadrature rule is applied as:

$$\int_{\Omega_m} B_{ijk}[x^n(\eta), \xi]\; M^\beta(\eta)\; d\Omega_m$$

$$= \int_{-1}^{1}\int_{-1}^{1}\int_{-1}^{1} B_{ijk}[\underline{x}(\underline{\eta}),\underline{\xi}]\; M_\beta(\underline{\eta})\; J(\underline{\eta})\; d\eta_1\, d\eta_2\, d\eta_3 \qquad (3.14)$$

$$= \sum_{a=1}^{A}\sum_{b=1}^{B}\sum_{c=1}^{C} w^a w^b w^c B_{ijk}[x,\eta^{abc},\xi]\; M_\beta(\eta^{abc})\; J(\eta^{abc})$$

where the volume element and Jacobian are defined by:

$$d\Omega_m = J(\eta_1,\eta_2,\eta_3)\, d\eta_1\, d\eta_2\, d\eta_3$$

$$J(\eta_1,\eta_2,\eta_3) = \det\left(\frac{\partial x_i}{\partial \eta_j}\right), \qquad i,j = 1,3$$

The non-singular integration is then carried out in a straightforward manner using ordinary Gaussian integration formulae, with appropriate error control via cell subdivision.

The singular integration technique is selected by carefully studying the behavior of the kernel functions involved. For the volume integral in (3.13) which is singular of the order $1/r^2$, the adopted procedure of integration is as follows:

1. The curvilinear cell is transformed to a unit cell by using the isoparametric transformation.
2. Depending upon the location of the singular point, the cell is subdivided into three sub-cells, when the singularity is at a corner node, or four sub-cells, when the singularity is on the cell side.
3. Each sub-cell is then mapped into a unit cube.

Since the original integrand is singular of the order $1/r^2$, it becomes bounded in the transformed domain and, therefore, it can be evaluated accurately by selecting a suitable order of integration rule.

The singular integral involving the function B_{ipjk} is strongly singular (of order $1/r^3$) and the integrand is made bounded by excluding a neighborhood of the source point, in the form of a sphere, and mapping the remaining curvilinear cell to a unit cell for integration using the quadrature formula. This cell is further sub-divided in a manner which reflects the order of the integrand involved.

A much more satisfactory procedure can be used to evaluate the singular contributions in the interior stress calculations, if an entire subregion is filled with cells. If the subregion is unrestrained, the surface tractions will be zero and the displacements can be easily calculated for the case of uniform initial stress distribution. The singular terms can be then easily calculated by summing up the contributions such that the stresses are zero at every nodal point.

In the present version of BEST3D both above mentioned procedures have been implemented.

3.3.2.4 ANISOTROPIC ELASTICITY Anisotropic materials are frequently called for in the design of the hot section of a gas turbine engine. The material anisotropy typically arises either from a controlled casting operation (as with directionally solidified or single crystal airfoils) or from processing operations applied to an originally isotropic material. The anisotropic material classes presently of major interest in the analysis of gas turbine engine structures are transversely isotropic (directionally solidified castings) and cubic (single crystal castings). In addition, local nonlinear deformation may induce anisotropy in an otherwise isotropic material.

As pointed out previously (Ref. 2) the application of the boundary element method to the elastic analysis of anisotropic materials requires, as a minimum:

- The point load solution for the (generally oriented) anisotropic material must be calculable.
- The surface stress calculation must be appropriately modified.

In addition, application to meaningful problems requires the development of a particular integral for centrifugal loads. Further, if nonlinear analysis of such materials is to be considered, it must also be possible to calculate the higher order kernels required for the evaluation of interior stress and for the volume integration of initial stress.

The BEST3D surface stress routines were originally written to handle general anisotropic materials, and the required particular integral for centrifugal loading was developed during Task IIC. The major challenge in the efficient application of boundary element analysis to anisotropic materials is thus the development of suitable techniques for the calculation of the required kernel function values.

3.3.2.4.1 Analytical Kernel Representation The point load function (displacement kernel) for a general anisotropic material can be represented as a line integral,

$$U_{ij}(\underline{x}-\underline{y}) = \frac{1}{8\pi^2|\underline{x}-\underline{y}|}\oint K_{ij}^{-1}(\xi)\,ds \tag{3.15}$$

This equation defines the displacement in the i-direction at a point $\underline{x}$ due to the application of a point load in the j-direction at the point $\underline{y}$. The line integral is taken on the circle on the unit sphere which is perpendicular to the vector $\underline{x}-\underline{y}$. The integrand,

defined by,

$$K_{ij}(\xi) = C_{ijkm}\xi_k\xi_m \tag{3.16}$$

is the inverse of a matrix, whose entries are quadratic forms with coefficients which are the elastic constants of the (C_{ijkm}) of the material.

The ideal solution to the calculation of the point load function, and the required derivatives, is the reduction of the line integral to a closed form, elementary expression. In the case of an isotropic material, $|K_{ij}|$ is constant over the unit sphere. As a result the line integral simplifies considerably, leading finally to the familiar Kelvin point load solution.

In the case of anisotropy, the evaluation of (3.15) requires further consideration. Using Fourier transform techniques (Ref. 3), it is possible to develop an alternative representation of the point load solution as an integral in the complex plane,

$$U_{ij}(\underline{x} - \underline{y}) = \frac{1}{\pi}\int_{-\infty}^{+\infty} \frac{\mathcal{F}_{ij}(z)}{\mathcal{F}(z)}\,dz = U_{ij}(\underline{r}) \tag{3.17}$$

where z is derived from $\underline{\xi}$ by a change of variables to spherical polar coordinates. The denominator $\mathcal{F}(z)$ is a 6th order polynomial equation in z. Complex variable theory allows the representation of the point load solution in terms of the residues of the integrand at the zeroes of $\mathcal{F}(z)$ (the poles of the integrand).

In order for this representation to be useful in boundary element analysis it is necessary to solve the equation $\mathcal{F}(z) = 0$ explicitly, in terms of the elastic constants of the material, for an arbitrary orientation of the vector $\underline{x} - \underline{y}$. This can be done, trivially, for an isotropic material. For the important case of a directionally solidified material the problem is much more complex, but still solvable. In that case $\mathcal{F}(z)$ factors into the product of three quadratic expressions. The roots of each factor can therefore be calculated in terms of radicals, allowing the use of the residue theorem to produce a closed form solution in terms of elementary functions. A particularly useful form of this solution was developed in Ref. 4, and was, after considerable simplification, incorporated in BEST3D during Task IIC. The same authors have extended this work to produce a closed form, but very complicated, point load solution for two-phase transversely isotropic materials (Ref. 5).

3.3.2.4.2 Single Crystal Materials The other material class of primary interest in hot section components consists of cubic crystals (single crystal materials). These materials are defined by three material constants (C_{11}, C_{12}, C_{44}). Despite this seemingly simple structure , $\mathcal{F}(z)$ can be solved using radicals only for certain very special cases:

- $C_{11} - C_{12} - 2C_{44} = 0$ (isotropic)
- $C_{12} = -C_{44}$

- $\underline{x} - \underline{y}$ is aligned with a material axis.

The last of these special cases is not useful, because the evaluation of the point load solution is required for general orientations of $\underline{x} - \underline{y}$. Single crystal turbine engine materials satisfy neither of the first two conditions.

In order to apply boundary element analysis to single crystal materials it is, therefore, necessary to develop techniques for the efficient and accurate numerical approximation of the point load solution and its derivatives. There are three major categories of approximate representations which can be considered: series representations, tabulation/interpolation of kernel function values and matrix techniques. These techniques will be reviewed in the context of their suitability for boundary element analysis.

3.3.2.4.3 Series Representation In a series representation each term of the point load solution is represented as an infinite series of relatively simple functions, frequently the powers of an expansion parameter. A frequently used parameter for single crystal materials is $d = C_{11} - C_{12} - 2C_{44}$, the 'deviation' from isotropy. The coefficients in the expansion are chosen to give a good fit to the actual point load solution using only a few terms of the series representation. Such techniques are discussed in detail in Reference 3.

Three major disadvantages make these techniques unsuitable for use in boundary element analysis. First, accuracy is difficult to evaluate or control. In general the success of the approximation depends on how near the single crystal material is to an isotropic material. As Figure 3.1 indicates, aerospace single crystal alloys are relatively far removed from isotropic behavior. Second, the algebraic process required to evaluate the coefficients in the approximation is very complex. Finally, the derivatives of such representations typically lose further accuracy with every differentiation. Depending on the application, boundary element analysis requires from one to three derivatives of the basic point load solution. It would not be possible to maintain required accuracy using derivatives of a series representation.

3.3.2.4.4 Interpolation in Tabulated Data A second approach to the approximation of the single crystal point load function is the use of tabulated data together with suitable interpolation routines. This approach is described in some detail in Ref. 6. Briefly, it is possible to numerically evaluate the line integral in (3.15) to any required degree of accuracy. Further, the line integral depends only on the orientation of $\underline{x} - \underline{y}$. It is thus possible to tabulate the values of the line integral on the surface of the unit sphere, and to interpolate in the table to obtain the orientation dependence of intermediate points. Further, by differentiation of (3.15) and repeated use of the chain rule, it is possible to reduce any required derivative of the point load function to related, non-

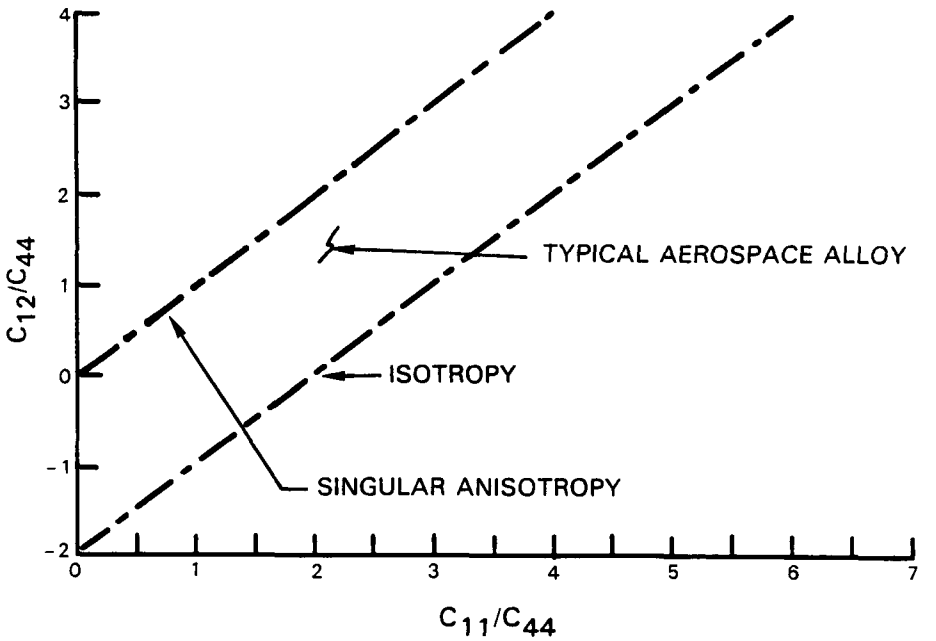

Figure 3.1: Relationship of Single Crystal Material to Isotropy

singular orientation dependent line integrals. These integrals can also be tabulated, with the same degree of accuracy as the point load function.

The method outlined has been implemented in a three-dimensional boundary element code, with generally excellent results. Analysis is significantly more costly than for an isotropic material because of the large amount of computation required for the interpolations. The penalty in computing time is a factor of approximately 1.9 compared to approximately 1.3 for the closed form directionally solidified kernel implemented in BEST3D.

In addition to the question of computing time the tabulation/interpolation technique has major disadvantages for use in a general purpose code, such as BEST3D. First, a great deal of data is involved. Using a 17x33 grid to cover the unit sphere, the point load table requires almost 3400 (double precision) words of storage. The first derivatives (required even for the boundary solution) require an additional 10,000 words. Second derivatives (required for interior stress calculation) require 30,300 words. Third derivatives (required for volume integral based plasticity) would require 90,000 more words. Second, the tables (produced and stored by a separate program) are based on a specific set of material constants. If the material properties are changed, then the entire table must be regenerated. Finally the questio of temperature dependent material properties is extremely difficult. Data storage requirements are, of course, multiplied by the number of temperature values

in the data base. More importantly, there is no reliable method for interpolating in the data base to obtain kernel function values at intermediate temperatures.

3.3.2.4.5 Matrix Formulation An alternative formulation can be given in terms of matrix algebra. This alternative formulation was initially developed in the field of solid state physics, in a context much more general than the simple construction of static point load solutions. The general technique can be applied to the complete equilibrium equation, including the inertia term. Further, more general singular distributions (for example, line loads and dislocations) can be considered, as can the presence of initial plastic strain. The possible application of the technique for the calculation of the single crystal point load solution is described below. The notation employed is generally that of K. Malen (Ref. 7).

In the static case, the equilibrium equation takes the form,

$$\sigma_{ij,j} = -f_i \tag{3.18}$$

with the stress-strain relation,

$$\sigma_{ij} = C_{ijkl}\beta_{kl}$$

and

$$U_{k,l} = \beta_{kl}$$

Taking Fourier transforms and substituting for β_{ik} in terms of U_k, the following equations are obtained:

$$\begin{aligned} ik_j\tilde{\sigma}_{ij} &= -\rho\omega^2\tilde{U}_i - \tilde{f}_i \\ \tilde{\sigma}_{ij} &= ik_l C_{ijkl}\tilde{U}_k \end{aligned} \tag{3.19}$$

To simplify the calculation of the point load solution a new coordinate system is introduced. The vector $\underline{\tau}$ is a unit vector in the direction from the load point to the field point. The unit vectors $\underline{m}$ and $\underline{n}$ are then chosen to complete a right handed orthogonal coordinate system. The vector from the load point to an arbitrary point in space can then be represented as:

$$\underline{k} = k(\alpha\underline{m} + \beta\underline{n} + \gamma\underline{\tau})$$

with,

$$k = |\underline{k}|$$

Adopting the convention that

$$(kk)_{ik} = k_j C_{jikl} k_l$$

defining

$$p = \beta/\alpha$$

$$q = \gamma/\alpha$$

and taking E to be the 6x6 identity matrix, the equilibrium equations can be written in matrix form as

$$(N - pE + qA)\tilde{\zeta} = k^{-2}\alpha^{-2}Q \tag{3.20}$$

where the vectors $\tilde{\zeta}$ and Q are defined as

$$\begin{array}{lll} \tilde{\zeta}_i = \tilde{U}_i & Q_i = 0 & i = 1,3 \\ \tilde{\zeta}_i = (\alpha k)^{-1} n_j \tilde{\sigma}_{ij} & Q_i = -i\tilde{f}_i & i = 4,6 \end{array}$$

and

$$N = \begin{bmatrix} -(nn)^{-1}nm & -i(nn)^{-1} \\ -i(mm) + i(mn)(nn)^{-1}(nm) & -(mn)(nn)^{-1} \end{bmatrix}$$

$$A = \begin{bmatrix} -(nn)^{-1}(n\tau) & 0 \\ -i[(m\tau) + (\tau m) + p(\tau n) + q(\tau\tau)] + i(mn)(nn)^{-1}(n\tau) & 0 \end{bmatrix}$$

In the case of a point load, $f_i = F_i\delta(r)$, so that,

$$\tilde{f}_i = F_i$$

and the vector Q is independent of k, simplifying to

$$\begin{array}{ll} Q_i = 0 & i = 1,3 \\ Q_i = -iF_i & i = 4,6 \end{array}$$

leading to the equation

$$\tilde{\zeta}(p,q) = (N - pE + qA)^{-1}Q \tag{3.21}$$

Fourier inversion leads to an expression for $\tilde{\zeta}_i$ in physical space in terms of the eigenvalues of $(N - pE)$.

$$\zeta(\underline{r}) = \frac{i}{4\pi r}\sum_{\nu=1}^{6} \pm \left[\frac{Adj(N - pE)Q}{\frac{\partial}{\partial p}|N - pE|}\right]_{p=p_\nu, q=0} \tag{3.22}$$

The first three components of this vector are the Cartesian components of displacement at $\underline{r}$ due to the application of the point load at the origin. The plus sign in this equation is used when $\Im(p_\nu) > 0$ and the minus sign when $\Im(p_\nu) < 0$. While there is a considerable amount of calculation required for the evaluation of this expression, all of it involves straightforward matrix operations. Even the extraction of the eigenvalues of the 6x6 matrix $(N - pE)$ can be performed using standard software packages. Further, in the case of the single crystal material it will be possible to considerably simplify the calculations involved in this evaluation. Evaluation of higher order kernels will be carried out by differentiation of the matrix form of the displacement kernel. Although additional terms are generated , the basic eigenvalue problem remains the same for the higher order kernels.

The utilization of the matrix formulation for evaluation of anisotropic point load solutions has several major advantages:

1. The need for the storage and manipulation of large, pre-calculated kernel function tables is eliminated.

2. Kernel function evaluations can always be done using correct material properties, eliminating the need to define a temperature interpolation at the kernel function level.

3. Accuracy will be easier to control, since no numerical integration is required in the kernel function evaluation. The only potentially sensitive operation is the solution of the 6x6 eigenvalue problem, but the currently available algorithms allow this to be done with very high accuracy, without user or programmer intervention.

It is anticipated that the calculations involved can be streamlined sufficiently to allow the exact calculation of kernel function values at all required points. In the event that this cannot be done, it is planned to calculate the exact values, for a given source point location, at a suitable set of points (normally the geometric nodes) on a single surface element. Interpolation using the normal isoparametric shape functions will then be used to provide a good approximation to the kernel function values at individual integration points.

3.3.2.5 APPLICATION OF PARTICULAR INTEGRALS The early development of the boundary element method, especially in three dimensions, concentrated on the static elastic analysis of homogeneous materials. Recent developments, including work done in the present program, have demonstrated that the method is applicable to both anisotropic elastic analysis and inelastic analysis. In particular the present version of BEST3D includes provision for the analysis of directionally solidified materials and for inelastic analysis. It is planned to incorporate the kernel functions for single crystal materials during the final year of the program, as outlined in 3.3.2.4.

The major remaining technical obstacle to the incorporation of the three dimensional boundary element method in the aerospace design process is the difficulty encountered in efficiently handling continuously inhomogeneous (generally temperature dependent) elastic material properties, and, to a lesser extent, thermal stress. Multi-material problems can be effectively handled by substructuring, or (potentially) the use of special kernel functions. Situations with continuously variable elastic properties and/or time dependent temperature distributions have required the use of a subsidiary volume discretization and volume integration. These procedures are discussed in the first two Annual Reports (NASA CR-174700 and NASA CR-175060). A two-dimensional application to elastic inhomogeneity is presented in Ref. 8.

While this technique is capable, in principle, of providing the solution to very general three-dimensional problems it is not suitable for routine application in an aerospace design

environment, for two major reasons:

1. The creation of the volume discretization, while less demanding than in finite element analysis, still imposes a significant additional burden on the analyst.

2. The extensive volume integration involved is extremely expensive. Further, despite significant advances made during Task IVC (3.3.2.3) it remains very difficult to guarantee sufficient accuracy in the volume integrals, particularly when thermal loading is important.

Plasticity analysis is also affected by the costs associated with volume integration and volume discretization, although the cost of finite element plasticity analysis makes the expense associated with volume discretization in the boundary element method appear less significant. In addition, in many plasticity analyses the region of plastic behavior is quite constrained, helping to control both the size of the volume mesh and the associated costs.

The method developed during Task IVC is based on the well known fact that the solution to an inhomogeneous system of differential equations can be represented as the sum of a complementary solution satisfying the homogeneous equation and a particular solution satisfying the inhomogeneous equation. In the case of the stress analysis of a solid the equilibrium equations can be written as:

$$\mu_{i,jj} + (\lambda + \mu)u_{j,ji} - \lambda\epsilon^0_{kk,i} + 2\mu\epsilon^0_{ij,j} \tag{3.23}$$

or in operator form as:

$$L(u_i) = \lambda\epsilon^0_{kk,i} + 2\mu\epsilon^0_{ij,j} \tag{3.24}$$

where λ and μ are reference moduli (constant throughout a substructure) and ϵ^0_{ij} is the initial strain, generally nonzero throughout the part, due to thermal, inelastic and inhomogeneity effects. The initial strain is written as:

$$\epsilon^0_{ij}(x) = H_{ijkl}(x)\sigma_{kl}(x) - H^0_{ijkl}\sigma_{kl}(x) + \delta_{ij}\Delta T(x)\alpha(x) \tag{3.25}$$

where H, H^0 and $\tilde{H}(= H - H^0)$ are the reference, local and deviation compliance tensors, respectively. If a particular solution to (3.24) can be found, then the physical solution can be represented as:

$$u^{physical} = u^{complementary} + u^{particular}$$

and a boundary integral equation can be derived for the complementary solution. Expressing the displacements and tractions of the complementary solution in terms of the

physical solution and the (known) particular solution then allows the development of a boundary equation for the physical solution:

$$c_{ij}u_j - \int_S [G_{ij}t_i - F_{ij}u_i]\,dS = c_{ij}u_i^P - \int_S [G_{ij}t_i^P - F_{ij}u_i^P]\,dS \qquad (3.26)$$

This is then reduced to algebraic form in the usual manner. A similar technique is already employed in BEST3D for the solution of problems with centrifugal loads.

Application of this method to the solution of problems of inhomogeneity and thermal stress will depend on the development of suitable particular solutions to be used for the representation of the initial strain fields involved.

It can be shown (Ref. 9) that (assuming appropriate continuity and differentiability conditions), if a potential function g is chosen so that:

$$\epsilon_{ij}^0 = g_{ij,kkmm}$$

then a Galerkin vector F, defined by:

$$(1-\nu)F_i = \lambda g_{kk,i} + 2\mu g_{ij,j}$$

will lead to a displacement field which is a particular solution of (3.24). Any solution of the inhomogeneous biharmonic equation thus becomes a possible starting point for a particular solution of (3.24). There are two general classes of suitable functions:

1. Domain functions, chosen to allow representation of a suitable variation of initial strain throughout an entire substructure or part.

2. Point based functions, which take on their largest value at a particular boundary or interior point and decay as a function of the distance from that point.

Domain functions are particularly suitable for the representation of thermal strain, whose variation is usually known *a priori*, while point based functions appear more suitable for the representation of initial strain due to inhomogeneity. If necessary, both types of representations can be used in a single analysis.

Both forms of initial strain approximation discussed above are continuous and nonzero everywhere in three-dimensional space. An additional class of representations exists, in which the nonzero initial strain distribution is restricted to a small volume of space. This class is particularly useful in the representation of holes, without explicit modelling. It will be discussed further in 3.3.2.6.

The remainder of this section outlines one possible algorithm for the treatment of the combined thermal and mechanical loading of a structure with temperature dependent

elastic properties. In this case the initial strain is:

$$\epsilon^0_{ij} = \tilde{H}_{ijkl}\sigma_{kl} + \delta_{ij}\alpha\Delta T \tag{3.27}$$

Suitable functions are chosen for the approximation of the thermal strain (typically domain functions $\hat{M}_n$, with weights ψ^n_{ij}), and the inhomogeneity strain (typically point based functions M_m, with weights ϕ^n_{ij}). The approximation of initial strain is written as:

$$\epsilon^0_{ij} = \sum_{n=1}^{\infty} \hat{M}_n \psi^N_{ij} + \sum_{m=1}^{\infty} M_m \phi^M_{ij} \tag{3.28}$$

It should be noted that the sums in the above equations may be either over sets of points (surface and interior) or over a set of terms not specifically associated with geometric locations in the structure.

The initial strain approximations lead, through appropriate differentiation and use of the stress-strain relationship, to particular solutions for the thermal and inhomogeneity initial strains. It is important to note that the particular solutions are linear in ψ^n_{ij} and ϕ^m_{ij}, respectively .

If the physical solution is represented as:

$$u = u^c + u^p$$

then the usual methods allow the derivation of the algebraic form of the boundary integral equation for the complementary solution:

$$A\underline{x}^c = B\underline{y}^c$$

where $\underline{x}$ is the vector of unknowns and $\underline{y}$ the vector of known displacements and tractions. This can be rewritten in terms of the physical unknowns as:

$$A\underline{x} = B\underline{y} + AQ\underline{\phi} + A\hat{Q}\underline{\psi} \tag{3.29}$$

A similar development allows representation of the stress, at interior or boundary points, as:

$$\underline{\sigma} = C\underline{x} + D\underline{y} + CR\underline{\phi} + C\hat{R}\underline{\psi}$$

The vector of initial strains due to inhomogeneity can then be written as:

$$\underline{\epsilon}^0 = \tilde{H}\underline{\sigma} = \tilde{H}(C\underline{x} + D\underline{y}^c + CR\underline{\phi} + C\hat{R}\underline{\psi})$$

and since,

$$\underline{\phi} = P\underline{\epsilon}^0$$

the equation

$$\underline{\phi} = P\tilde{H}(C\underline{x} + D\underline{y}^c + CR\underline{\phi} + C\hat{R}\underline{\psi}) \tag{3.30}$$

is obtained.

These equations can be written in partitioned matrix form as:

$$\begin{bmatrix} A & AQ \\ PHC & PHCR \end{bmatrix} \begin{bmatrix} x \\ \phi \end{bmatrix} = \begin{bmatrix} r_1 \\ r_2 \end{bmatrix}$$

In this system the matrices A and C are the usual static boundary element matrices. All of the other matrices involved are related either to the stress-strain relationship or to the initial strain approximations, and require no integration, only function evaluations, for their construction.

The linear equation system can either be solved directly or the weights, $\underline{\phi}$, can be eliminated as a first step, leading to variable stiffness formulation.

An entirely similar formulation can be developed for nonlinear analysis, including thermal effects. Initial versions of such a nonlinear algorithm have been developed and are being evaluated and refined in BEST3D.

In summary, the use of particular integrals now offers the realistic possibility of analyzing structures with thermal loading, inhomogeneity and nonlinear response. Input definition is significantly simplified, since no interior connectivity is required. Since volume integration is no longer required, the highly singular 4th rank kernels are completely avoided, as is the (highly singular) volume integration of the third rank kernels. The only direct attention required to the interior of the structure is the possible placement of points for use in the approximation of initial strain.

3.3.2.6 REPRESENTATION OF HOLES/CAVITIES Turbine engine hot section components frequently contain arrays of holes, usually to allow the passage of cooling air. On occasion arrays of holes are also used to reduce component weight. In addition, cracks may be found in such components, frequently originating from cooling holes or other structural details.

Clearly, one method of solution for such problems is the modelling of the hole or crack surface(s) using boundary elements. This method has been shown to accurately define stress concentration and fracture mechanics parameters in complex three-dimensional structures. Good agreement has been demonstrated between nonlinear experimental and boundary element results in notches (Ref. 2). This direct modelling method has the advantage of providing very detailed and accurate results near the hole or crack. If only a single such discontinuity is to be studied, the additional analysis cost is usually not

excessive. If, however, an array of discontinuities is present in a part, direct modelling will no longer be feasible.

Three alternative methods are under active consideration for incorporation in BEST3D for the representation of holes and/or cracks without detailed boundary element modelling, a hybrid surface integral/boundary element method, the development of approximate kernel functions and the use of exact or approximate solutions for inclusions.

3.3.2.6.1 Surface Integral/Boundary Element Hybrid The surface integral method (Ref. 10 and 11) allows the modelling of cracks in an unbounded solid using a distribution of point force dipoles on the crack surface. Dipole strengths are assigned at suitably chosen points on the crack surface (not required to be planar). The resulting integral equations are numerically solved at a set of collocation points on the crack surface. While points must be defined on the crack surface, no connectivity definition is required. The upper and lower crack surfaces are not modelled separately. The surface integral method has been successfully coupled to the finite element method for the solution of problems involving cracks in finite bodies (Ref. 12). The coupling involves a finite element solution for the uncracked body and a surface integral solution for the actual crack geometry in an unbounded solid. The two solutions are coupled by enforcing displacement compatibility and equilibrium on the external boundary and the crack surface.

A similar coupling between the surface integral and boundary element methods is clearly feasible. In this case the coupling will be made by calculating crack surface tractions using the boundary element interior stress identity.

3.3.2.6.2 Approximate Kernel Functions A second approach involves the construction of approximate kernel functions which include the presence of one (or more) holes or cracks. These approximate kernel functions can be generated by the following process:

1. A standard boundary element model is built for the desired cavity shape. The system matrix corresponding to the exterior problem is built and decomposed.

2. The tractions on the cavity surface due to an arbitrarily located point force are calculated. The negative of these tractions is applied to the cavity surface, and the decomposed system matrix is used to solve for the displacements on the cavity surface.

3. The boundary element interior displacement and stress identities are used to calculate the point load solution at an arbitrary point in the exterior of the cavity.

The considerable geometric symmetry which exists for many common hole shapes (cylinder, sphere, ellipsoid) can greatly simplify the calculations. The greatest potential disadvantages of this approach are its numerical complexity and the difficulty of controlling accuracy when the source point is near the hole. The method would become quite cumbersome if multiple holes were required in a single subregion. This method does, however, share with the surface integral method the ability to account directly for the variation of stress in the uncracked part within the region occupied by a hole.

3.3.2.6.3 Inclusion Solutions A final method, particularly suited to arrays of holes, is based on work done on the representation of inclusions in a solid (three-dimensional) body. The displacement field in the exterior of such an inclusion, of which a cavity is a special case, can be expressed (Ref. 13) either in terms of the transformation strain in the cavity, as:

$$u_i = \frac{e^T_{jk}}{8\pi(1-\nu)} \int_V \frac{dv}{r^2} g_{ijk}(\underline{l}) \tag{3.31}$$

or as:

$$u_i = \frac{p^T_{jk}}{16\pi\mu(1-\nu)} \int_V \frac{dv}{r^2} f_{ijk}(\underline{l}) \tag{3.32}$$

in terms of the transformation stress, where

$$f_{ijk} = (1-2\nu)(\delta_{ij}l_k + \delta_{ik}l_j) - \delta_{jk}l_i + 3l_il_jl_k$$

$$g_{ijk} = (1-2\nu)(\delta_{ij}l_k + \delta_{ik}l_j - \delta_{jk}l_i) + 3l_il_jl_k$$

and r is the length of the vector $\underline{l}$ joining a volume element dv to the point of observation.

The resulting stress field can be derived from the displacement field by differentiation. Evaluation of the displacement and stress fields by numerical integration is relatively straightforward. Routines for this evaluation can easily be designed to control accuracy based on the distance between the point at which the solution is to be calculated and the cavity. In particular, at locations remote from the cavity, the expression can be simplified to:

$$\begin{aligned} u_i &= \frac{V p^T_{jk} f_{ijk}}{16\pi\mu(1-\nu)r^2} \\ &= \frac{V e^T_{jk} g_{ijk}}{8\pi(1-\nu)r^2} \end{aligned}$$

In applying such solutions within the boundary element method, the transformation strain is chosen so that the sum of the transformation stress and the stress due to the boundary loads vanishes within the cavity.

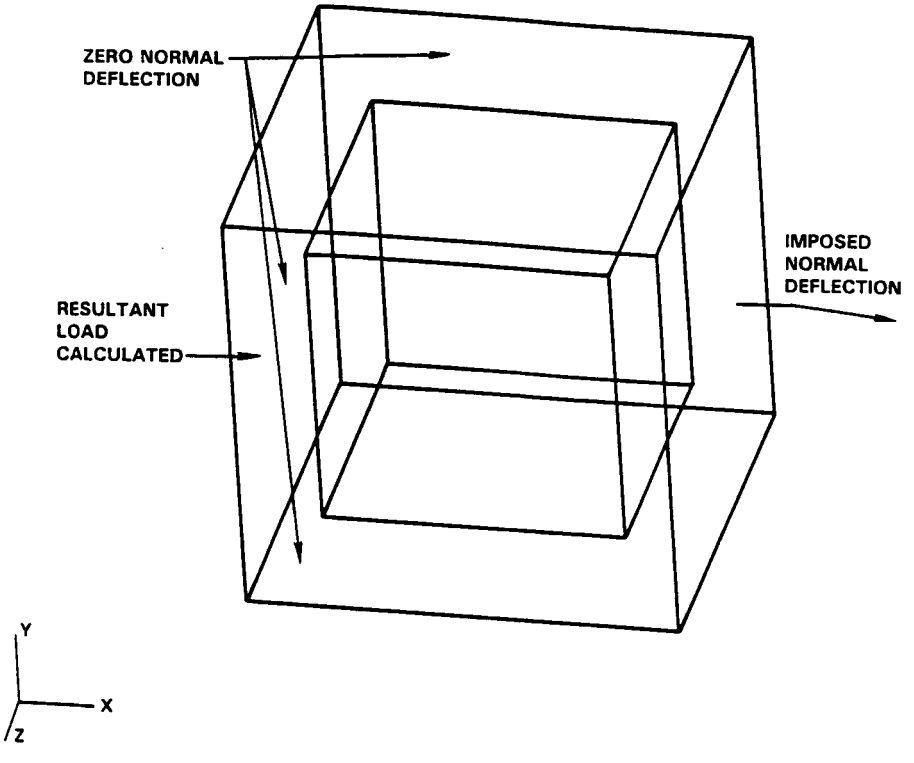

Figure 3.2: Cube Containing a Cavity

The decision to pursue this approach was guided by experience obtained during Task IIC, using a particular solution of this type. An exact (closed form) solution was obtained for an arbitrary, uniform transformation strain within a rectangular parallelepiped. Considerable experimentation was done to verify the practicality of the method outlined above. The test problem studied was that of a cubical cavity centered within a larger cube (Figure 3.2). The cube was subjected to an applied displacement along one axis. The transformation strain in the cuboid was defined by setting the integral of the total stress in the cuboid (using a 2x2x2 Gauss rule) to zero. The results obtained using the uniform transformation strain solution agreed well with results in which the cavity was modelled, over a wide range of cavity sizes. The load produced by the imposed deflection is shown in Figure 3.3. Even when the cavity occupied 50% of the total volume, the result of the approximate procedure produced a load only 8% lower than a complete modelling of the cavity. It is clear that the use of transformation strain solutions can correctly account for the overall load and displacement effects of a cavity, even at locations relatively near the cavity. Further, the results at relatively remote locations are quite insensitive to cavity

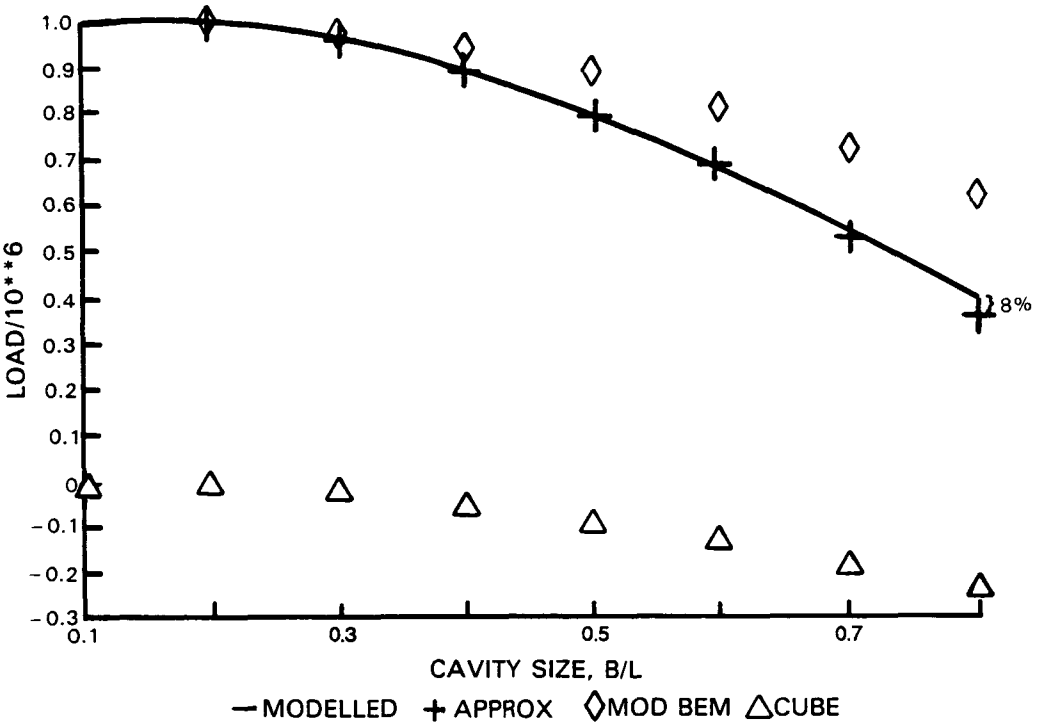

Figure 3.3: Load as a Function of Cavity Size

shape. Figure 3.4 shows the comparison between the loads due to a cubical cavity and a spherical cavity of equal volume. The load is seen to be insensitive to cavity shape even at a cavity size ratio of .4, for which the load is computed only 1.5 cavity dimensions away from the cavity boundary.

Further, even though the cuboid solution assumes uniform transformation stress, good results are obtained for local variation of field quantities near the hole. Figure 3.5 compares results obtained for the x-displacement (Poisson contraction for the solid cube) both by directly modelling of the cavity and by use of the cuboid solution. In this case the cavity size ratio is .6 and the displacements are calculated on a line passing within .125 cavity dimensions of the cavity. The presence of the cavity substantially modifies the Poisson contraction, which would be independent of axial location for a solid cube. The agreement between the results for the modelled and unmodelled cavities is excellent.

The success demonstrated using the simple cuboid solution gives considerable confidence in the ability to model arrays of discontinuities using closed form or approximate inclusion solutions derived from (3.31) and (3.32). The technique will be computationally efficient and will fit within the same general framework as the particular solution formulation for inhomogeneity and thermal stress.

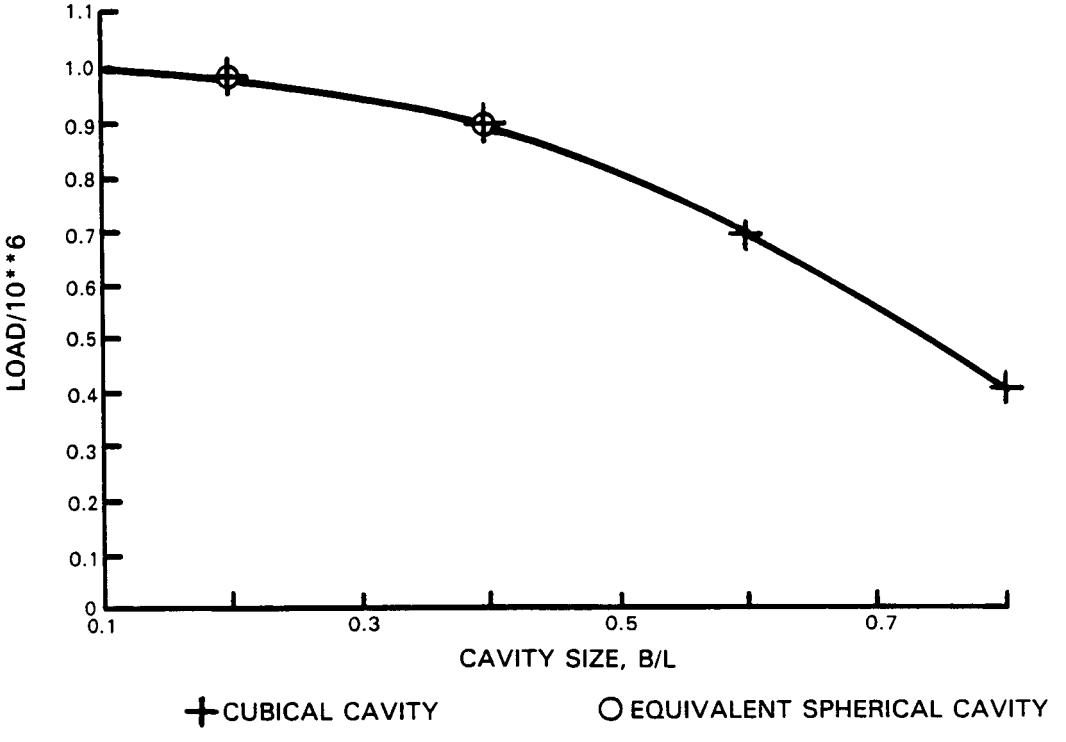

Figure 3.4: Effect of Cavity Shape on Load

The only significant drawback of the method is the assumption of a uniform transformation stress within each inclusion. This will become important only if the cavity is large enough that the stress varies significantly over the region occupied by the hole and if local results near the hole are required. In the short term this can be addressed by directly modelling a single hole in order to obtain the required local results. A more satisfactory long term solution would be the development of generalized versions of (3.31) and (3.32) allowing for variation of the transformation strain or stress.

3.3.2.7 GENERALIZED FUNCTIONAL REPRESENTATIONS The present version of the BEST3D program models part geometry using quadratic isoparametric surface patches. Displacement and traction over each patch are represented using either quadratic or linear isoparametric shape functions. Although such representations can give adequate definition of both geometry and field quantities for almost any real problem, there are several undesirable features:

1. The elements are not able to reproduce exactly a number of frequently used surface types, such as cylinders, spheres and ellipsoids;

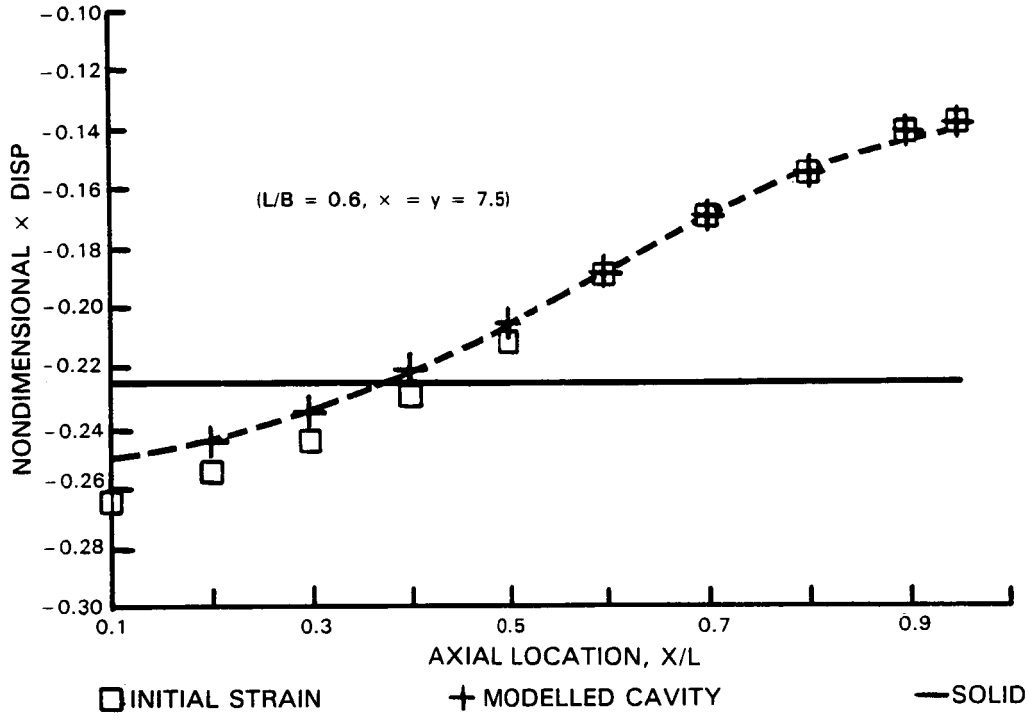

Figure 3.5: Accuracy of Response Near Cavity

2. The modeling of real parts using such elements requires considerable hand calculation or the writing of special purpose computer programs, in order to fit surface patches to the true geometry;

3. The elements are not entities used in the many geometric modeling systems which are, increasingly, being used for design purposes in the aerospace industries.

A number of solid modeling systems presently under development, or already commercially available, use rational b-splines (in two dimensions) and rational b-spline surfaces (in three dimensions) for the representation of surface geometry. In such a representation each coordinate is represented in the form:

$$\begin{aligned} S(s,t) &= (x(s,t), y(s,t), z(s,t)) \\ &= \frac{\sum_{i=1}^{n}\sum_{j=1}^{m} B_{i,k}(s) B_{j,l}(t) h_{ij} P_{ij}}{\sum_{i=1}^{n}\sum_{j=1}^{m} B_{i,k}(s) B_{j,l}(t) h_{ij}} \end{aligned} \tag{3.33}$$

where the P_{ij} and the h_{ij} are the control point values defining the geometry. The $B_{j,k}$ are a suitable set of basis functions, normally taken to be piecewise cubic. These representations possess the smoothness characteristic of real part geometry. Additionally, many

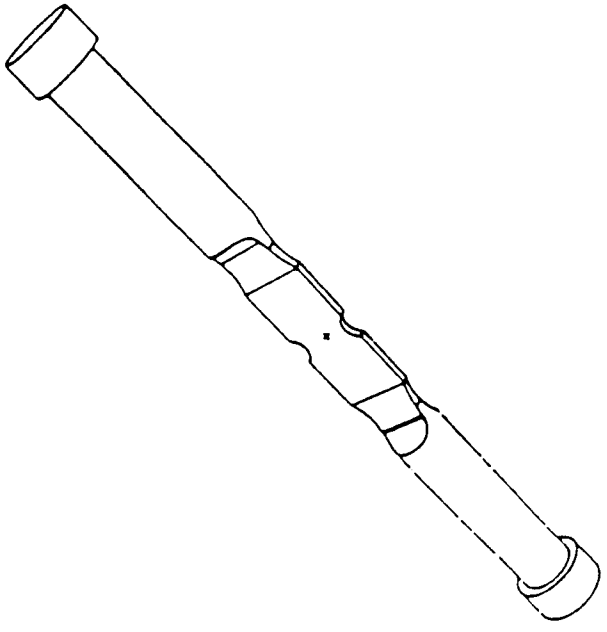

Figure 3.6: Geometric Model of Low Cycle Fatigue Specimen

types of geometric details can be exactly represented using b-splines. It is, therefore, possible to provide a very accurate geometry representation using only a few elements. As an example, the low cycle fatigue specimen shown in Figure 3.6 consists of only 26 rational b-spline surfaces. It was constructed in less than three hours using the CAEDS modeling system. Equally accurate representation of the same geometry using the current BEST3D modeling technology would require a minimum of 150 surface patches.

The evident advantages of the b-spline representation have made it important to determine whether such a representation can be successfully incorporated in a boundary element analysis. In order to carry out this experimentation as rapidly and efficiently as possible, a two-dimensional (plane stress) boudary element stress analysis code using rational b-splines to represent geometry, displacement and traction has been written. Key questions to be investigated include:

1. The numerical stability of the resulting equation system;

2. Sensitivity of the solution to the choice of collocation points;

3. Whether or not displacement compatibility must be enforced as an additional constraint at the break points between boundary segments.

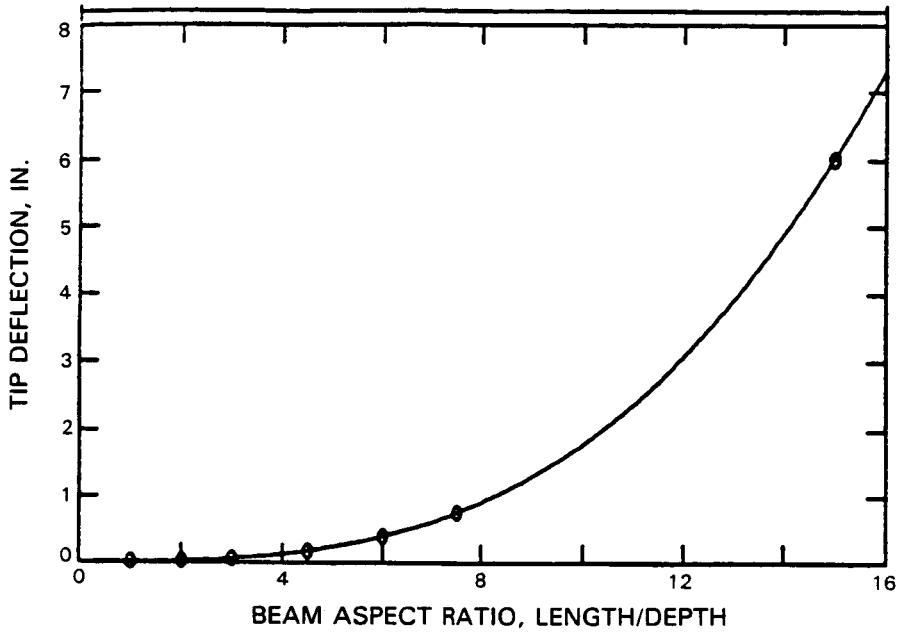

Figure 3.7: Beam Deflection ($\nu = 0$)

The results to date are promising, although considerable work remains to be done. The test problem currently being used is that of a cantilever beam subject to a (parabolically distributed) shear load on the free end. This problem has always been an exceptionally difficult one for boundary element codes using isoparametric elements, but should have an essentially exact solution within the function space of rational b-splines. As is shown in Figure 3.7, when Poisson's ratio is equal to zero, the spline based boundary element code gives excellent results over a wide range of beam aspect ratios. However, when Poisson's ratio is nonzero (Figure 3.8), the results gradually deteriorate as beam aspect ratio increases.

Investigation of the problem shows that the system equations are very poorly conditioned relative to the isoparametric formulation. The solution is extremely sensitive to the values of the off-diagonal terms in the traction kernel. Since the degree of sensitivity is the same for $\nu = 0$ and $\nu = .35$, the preliminary conclusion is that further attention is required to the accurate calculation of the traction kernel integrals. In addition, possible restructuring of the equation system to improve stability is being investigated.

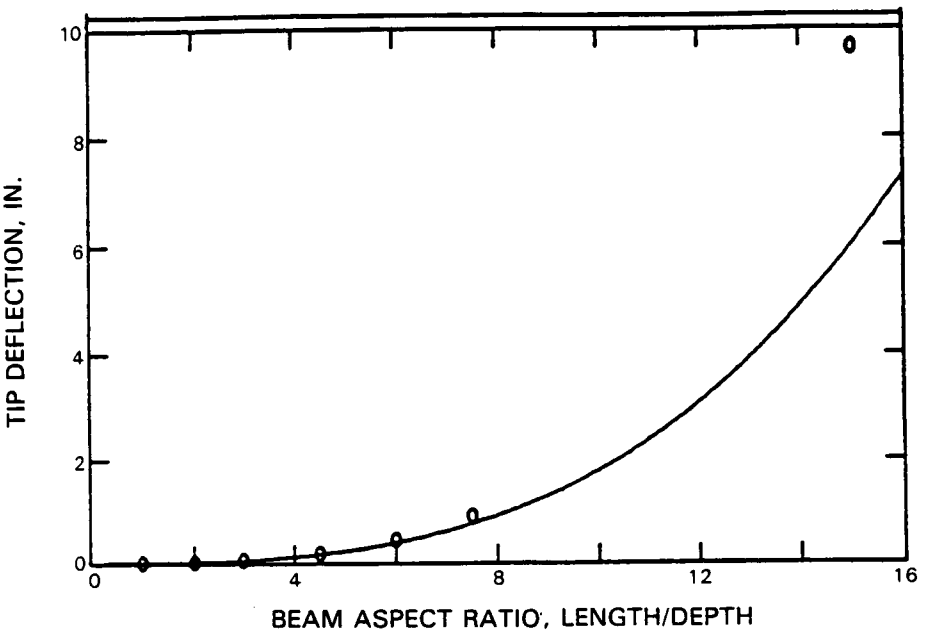

Figure 3.8: Beam Deflection ($\nu = .35$)

3.3.3 TRANSIENT AND DYNAMIC STRESS ANALYSIS

3.3.3.1 REVIEW Three-dimensional problems of elastodynamics were not attempted until recently principally because of enormous computing requirements and the formidable task of numerical implementation. In order to reduce the computation and complications involved, simplifications of the BEM formulation dictated by the nature of the problem to be solved have been developed by a number of researchers.

Dominguez (Ref. 17) simplified the steady-state dynamic kernel functions for the special case of periodic surface loading on rectangular foundations. He introduced simpler kernel functions to study the response of embedded rectangular foundations subjected to travelling waves. Karabalis and Beskos (Ref. 18) have done similar simplifications to the time domain transient boundary integral formulation. Yoshida, *et. al.* (Ref. 19) used a simplified BEM formulation for determining the response of a square foundation on an elastic halfspace, subjected to periodic loading and harmonic waves. Tanaka and Maeda (Ref. 20) have developed a Green's function for two-layered visco-elastic medium, and using this Green function in a simplified BEM formulation they numerically calculated the compliances for a hemispherical foundation. More complex problems involving the periodic response of piles and pile groups have been attempted by Sen, *et. al.* (Refs. 21-23) and Kaynia and Kausel (Ref. 24). They simplified the boundary integral formulation so that only displacement kernels are involved in the formulation. Some authors

have also introduced a potentially unstable method involving an 'auxiliary boundary' so that singular integration can be avoided. In all of the above works, the displacements and tractions are assumed to be constant over each surface element.

Recently, Rizzo, *et. al.* (Ref. 25) and Kitahara and Nakagawa (Ref. 26) have implemented the BEM formulation for steady-state elastodynamic problems in a general form. Rizzo also implemented both a mixed-transform inversion to obtain the response in the time domain and a technique for the problem of fictitious eigenfrequency in certain exterior problems with homogeneous boundary conditions. Kitahara and Nakagawa have introduced series expansion of the periodic kernels for the low frequency range, to obtain a stable solution at low frequencies.

In the present work, the direct boundary element formulations for periodic dynamic analysis and time-domain transient analysis have been implemented for problems involving isotropic, piecewise homogeneous (substructured), three-dimensional solids. These implementations are general and complete in all respects. In addition, for nonlinear, transient, dynamic analysis of three-dimensional solids, the direct boundary element formulation and its numerical implementation are presented for the first time.

3.3.3.2 FURTHER DEVELOPMENT OF THE ELASTODYNAMIC FORMULATION During the course of Task IVC several new features have been added to the dynamic stress analysis part of the code to improve results as well as the efficiency of numerical computations.

3.3.3.2.1 Built-in Symmetry Capabilities In obtaining numerical solutions, a built-in symmetry capability allows one to solve problems having geometric and loading symmetry by modeling only a part of the actual geometry. The major steps in this procedure are briefly explained as follows: If the geometry and the boundary condition are symmetric with respect to a plane (or a number of planes), then only that portion of the boundary which lies on one side of the plane (or planes) is modeled. The symmetry can be with respect to $y-z$ plane (half-symmetry), $y-z$ and $x-z$ planes (quadrantal symmetry), or $y-z$, $x-z$ and $x-y$ planes (octant symmetry). The effect of the unmodeled part of the boundary is included according to the following scheme: For all the field points, the contributions of the unmodeled portions to the matrices of coefficients F_{ij} and G_{ij} are accounted for by reflecting the modeled surface elements with respect to the plane (or planes) of symmetry and then integrating over the reflected elements (with proper normals). For source points on the plane (or planes) of symmetry the contributions are added up directly whereas for all other source points the correct signs of the contributions are determined by the directions associated with the field variables with respect to the plane (or planes) of symmetry. By avoiding the calculation of identical quantities, this

procedure shortens the time required to evaluate the matrices. In addition, it reduces the time required to solve the set of linear equations, because the system matrix is much smaller.

3.3.3.2.2 Linear Time Stepping and Interior Stress Calculations The direct boundary integral formulation for a general, transient, elastodynamic problem can be constructed by combining the fundamental point force solution of the governing equations (Stoke's solution) with Graffi's dynamic reciprocal theorem. Details of this construction can be found in Banerjee and Butterfield (Ref. 14). For zero initial conditions and zero body forces, the boundary integral formulation for transient elastodynamics reduces to:

$$c_{ij}(\underline{\xi})u_i(\underline{\xi},T) = \int_S [G_{ij}(\underline{x},\underline{\xi},T) * t_i(\underline{x},T) - F_{ij}(\underline{x},\underline{\xi},T) * u_i(\underline{x},T)]\, dS(x) \tag{3.34}$$

where

$$G_{ij} * t_i = \int_0^T G_{ij}(\underline{x},T;\underline{\xi},\tau)\, t_i(x,\tau)\, d\tau \tag{3.35}$$

$$F_{ij} * u_i = \int_0^T F_{ij}(\underline{x},T;\underline{\xi},\tau)\, u_i(x,\tau)\, d\tau \tag{3.36}$$

are Reimann convolution integrals and $\underline{\xi}$ and $\underline{x}$ are the space positions of the receiver (field point) and the source (source point). The fundamental solutions G_{ij} and F_{ij} are the displacements and tractions at a point x and at a time T due to a unit force vector acting at a point $\underline{\xi}$ at a time τ. Equation (3.34) represents an exact formulation involving integration over the surface as well as the time history. It should also be noted that this is an implicit time-domain formulation because the response at time T is calculated by taking into account the history of surface tractions and displacements up to and including the time T. Furthermore, equation (3.34) is valid for both regular and unbounded domains.

Once the boundary solution is obtained, the stresses at the boundary nodes can be calculated without any integration by using the scheme described for the static case. For calculating displacements at interior points equation (3.34) can be used with $c_{ij} = \delta_{ij}$ and the interior stresses can be obtained from

$$\sigma_{ij}(\underline{\xi},T) = \int_S [G^{\sigma}_{ijk}(\underline{x},\underline{\xi},T) * t_i(\underline{x},T) - F^{\sigma}_{ijk}(\underline{x},\underline{\xi},T) * u_i(\underline{x},T)]\, dS(x) \tag{3.37}$$

The functions G^{σ}_{ij} and F^{σ}_{ij} in the above equation are too complex to be listed here.

In Task IVC constant time stepping was used to obtain the transient dynamic response. It was found to be more efficient to use a linear time variation of u and t on the boundaries.

In this case:

$$u_i(\underline{x},\tau) = \sum_{n=1}^{N}[\overline{M}_1\ u_i^{n-1}(\underline{x}) + \overline{M}_2\ u_i^n(\underline{x})] \tag{3.38}$$

$$t_i(\underline{x},\tau) = \sum_{n=1}^{N}[\overline{M}_1\ t_i^{n-1}(\underline{x},\tau) + \overline{M}_2\ t_i^n(\underline{x})] \tag{3.39}$$

where $\overline{M}_1$ and $\overline{M}_2$ are the time functions, and are of the form:

$$\overline{M}_1 = \frac{\tau_n - \tau}{\Delta T}\phi_n(\tau) \tag{3.40}$$

$$\overline{M}_2 = \frac{\tau - \tau_{n-1}}{\Delta T}\phi_n(\tau) \tag{3.41}$$

For illustration purposes, consider the boundary integral equation for the first time step, i.e.

$$c_{ij}u_i(\xi,T_1) - \int_{T_0}^{T_1}\int_S [G_{ij}t_i - F_{ij}u_i]\,dS\,d\tau = 0 \tag{3.42}$$

The time integration in equation 3.42 by utilizing 3.39 is done analytically. After the usual numerical integration and assembly process, the resulting system equation is of the form:

$$[A_2^1][X^1] - [B_2^1][Y_1] + [A_1^1][X^0] - [B_1^1][Y^0] = 0 \tag{3.43}$$

where:

- A and B are matrices related to the unknown and known field quantities, respectively:
- X and Y are the vectors of unknown and known field quantities, respectively:
- for X and Y the superscript denotes the time:
- for A and B the superscript denotes the time step at which they are calculated, and the subscript denotes the local time nodes (1 or 2) during that time-stepping interval.

Since all the unknowns at time $T = 0$ are assumed to be zero, equation 3.43 reduces to:

$$[A_2^1][X^1] = [B_2^1][Y^1] + [B_1^1][Y^0] \tag{3.44}$$

For second time step, the assembled system equation has the form

$$[A_2^1][X^2] - [B_2^1][Y^2] + [A_1^1][X^1] - [B_1^1][Y^1] = -[A_2^2][X^1] + [B_2^2][Y^1] - [A_1^2][X^0] + [B_1^2][Y^0] \tag{3.45}$$

As in the constant time variation scheme, only the matrices on the right hand side of equation 3.45 need be evaluated. However, one needs to integrate and assemble four matrices at each time step as compared to two in the case of constant time variation. This can be done with only a small increase in computing time by integrating all the kernels together and then assembling all the matrices together. Equation 3.45 can be rearranged such that:

$$[A_2^1][X^2] = [B_2^1][Y^2] - [A_1^1 + A_2^1][X^1] - [B_1^1 + B_2^2][Y^1] + [B_1^2][Y^1] \tag{3.46}$$

In the above equation, all the quantities on the right hand side are known. Therefore, the unknown vector X^2 at time T_2 can be obtained by solving the above equation.

Thus, for the present case, the boundary integral equation 3.46 can be written in discretized form as:

$$[A_2^1][X^N] - [B_2^1][Y^N] = -\sum_{n=2}^{N}[[A_2^n + A_1^{n-1}][X^{N-n+1}] - [B_2^n + B_1^{n-1}][Y^{N-n+1}] + [B_1^n][Y^0]] \tag{3.47}$$

or

$$[A_2^1][X^N] = [B_2^1][Y^N] + [R^N] \tag{3.48}$$

It is of interest to note that, if time interpolation functions $\overline{M}_1$ and $\overline{M}_2$ are replaced by $\overline{M}_1 = \overline{M}_2 = 0.5\phi_n(\tau)$, the time stepping scheme for linear variation can be used for the case of constant variation with averaging between the local time nodes.

3.3.3.3 EXTENSION TO NONLINEAR TRANSIENT DYNAMICS In this section, a direct boundary element formulation and its numerical implementation for nonlinear, transient, dynamic analysis of three-dimensional, deformable solids of arbitrary shape and connectivity is presented. The formulation is based on an initial stress approach, and is the first of its type in the field of boundary element analysis. The nonlinearity considered in this analysis is that due to the nonlinear constitutive relations, i.e. material nonlinearity. The boundary integral equations are cast in an incremental form, and thus, elasto-plastic relations of the incremental type are used for material description. These equations are solved by using a time-stepping algorithm in conjunction with an iterative solution scheme to satisfy the constitutive relations. The resulting algorithm is an unconditionally stable implicit scheme. However, the size of the time step that can be used is restricted by the size of the elements used for modelling the surface of the problem under consideration.

The direct boundary integral formulation for a nonlinear, transient, dynamic problem, based on an initial stress approach, can be constructed by following a procedure similar to the one that has been used for a nonlinear static problem (Ref. 14). Under zero initial

conditions and zero body forces, the boundary integral equation for nonlinear transient dynamics is of the form:

$$\begin{aligned} c_{ij}u_i(\underline{\xi},T) &= \int_S [G_{ij}(\underline{x},\underline{\xi},T) * t_i(\underline{x},T) - F_{ij}(\underline{x},\underline{\xi},T) * u_i(\underline{x},T)]\, dS(\underline{x}) \\ &\quad + \int_V B_{ilj}(\underline{x},\underline{\xi},T) * \sigma^0_{il}(\underline{x},T)\, dV(\underline{x}) \end{aligned} \tag{3.49}$$

where $*$ denotes convolution, and

- $\underline{\xi}$ and $\underline{x}$ are the space positions of the receiver (field point) and the source (source point), respectively:
- σ^0_{ij} is the initial stress tensor:
- V denotes the interior of the body:
- the fundamental solutions G_{ij}, F_{ij} and B_{ilj} are displacements, tractions and strains due to an impulse in an infinite solid.

Assuming all the field quantities to have a zero value at time $T = 0$, the boundary integral equation 3.49 can be written in an incremental form as follows:

$$\begin{aligned} c_{ij}(\underline{\xi})\Delta u_i(\underline{\xi},T) &= \int_S [G_{ij}(\underline{x},\underline{\xi},T) * \Delta t_i(\underline{x},T) - F_{ij}(\underline{x},\underline{\xi},T) * \Delta u_i(\underline{x},T)]\, dS(\underline{x}) \\ &\quad + \int_V B_{ilj}(\underline{x},\underline{\xi},T) * \Delta\sigma^0_{il}(\underline{x},T)\, dV(\underline{x}) \end{aligned} \tag{3.50}$$

where Δ denotes the incremental quantity.

The stress increment at an interior point $\underline{\xi}$:

$$\begin{aligned} \Delta\sigma_{jk}(\underline{\xi},T) &= \int_S [G^{\sigma}_{ijk}(\underline{x},\underline{\xi},T) * \Delta t_i(\underline{x},T) - F^{\sigma}_{ijk}(\underline{x},\underline{\xi},T) * \Delta u_i(\underline{x},T)]\, dS \\ &\quad + \int_V B^{\sigma}_{iljk}(\underline{x},\underline{\xi},T) * \Delta\sigma^0_{il}(\underline{x},T)\, dV + J_{iljk}\Delta\sigma^0_{il}(\underline{\xi},T) \end{aligned} \tag{3.51}$$

can be obtained by taking derivatives of equation 3.49 and using the constitutive relationships

$$\Delta\sigma_{ij} = D_{ijkl}\Delta\epsilon_{kl} - \Delta\sigma^0_{ij}$$

The functions G^{σ}_{ijk}, F^{σ}_{ijk}, B^{σ}_{iljk} and J_{iljk} are similar to their static counterparts except that some of the terms involve $(t - r/c_p)$ and $(t - r/c_s)$, the retarded times for pressure and shear waves, respectively.

In (3.51), the volume integral must be evaluated in the sense of $(V - V_\epsilon)$ as $V_\epsilon \rightarrow 0$ as discussed in section 3.3.2.2. The tensor J_{iljk} is the jump term derived from the analytical treatment of the integral over V_ϵ. This jump term is the same as that of static plasticity and is independent of the size of the exclusion V_ϵ, provided the initial stress distribution is locally homogeneous.

The equations for incremental stresses cannot be constructed at the boundary points by taking the field point, $\underline{\xi}$, in equation 3.51 to the surface, due to the strongly singular nature of the integrals involved. However, the equations for incremental stresses at boundary points can be constructed by using a scheme similar to that described for the quasi-static nonlinear problem. Thus the stresses at a boundary point can be obtained from:

$$\Delta\sigma_{jk}(\underline{\xi}^b, T) = \overline{G}^{\sigma}_{ijk}\Delta t_i(\underline{\xi}^b, T) - \overline{F}^{\sigma}_{ijk}\Delta u_i(\underline{\xi}^b, T) - \overline{B}^{\sigma}_{iljk}\Delta\sigma^0_{il}(\underline{\xi}^b, T) \qquad (3.52)$$

It should be noted that the above equation is free of any integration and time convolution.

In dynamic plasticity, the choice of an appropriate constitutive model depends largely on the material properties and the loading conditions of the problem in hand. For this reason various constitutive models have been used for dynamic plasticity. For simplicity in the present analysis, the Von Mises model with isotropic variable hardening is used. The use of any other constitutive equations within the present formulation will not cause any difficulty, as long as the evoluton of $\Delta\sigma^0_{il}$ can be obtained.

3.4 COMPUTER PROGRAM DEVELOPMENT

3.4.1 INTRODUCTION

The computer program BEST3D was developed during Tasks IC and IIC to provide a tool for applying the three-dimensional boundary element method to the structural analysis of gas turbine engine hot section components. The program, described in detail in the First (NASA CR-174700) and Second (NASA CR-175060) Annual Status Reports, was designed to accommodate structures with very general geometry and loading. Further it was clear that additional capabilities would be developed for BEST3D over a period of several years. For this reason the program was designed so that the anticipated capabilities could be incorporated within the original framework and data structure of BEST3D, without requiring major recoding of existing capabilities.

During Task IVC a number of new capabilities have been incorporated in BEST3D. The basic structure of the program remains, however, very similar to that of the original version. The major changes and additions made to the code during Task IVC, or presently in progress, are described in the following sections.

3.4.2 GLOBAL PROGRAM STRUCTURE

The major changes in the overall structure of BEST3D are:

- The incorporation, in the static analysis, of a branch for natural frequency and mode shape calculations.
- Addition of an additional nonlinear solution sequence (variable stiffness plasticity).
- The implementation, in a test version of BEST3D, of a nonlinear dynamics capability.

The overall structure of BEST3D at the end of Task IVC is shown in Figure 3.9. The program consists of a common input section, followed by three branches, for static, forced response and transient analysis. The static analysis branch is the model for the entire code, since the other branches largely employ generalized forms of the same algorithms used in the static analysis. The branch used for natural frequency/mode shape calculation is actually part of the static analysis loop.

ORIGINAL PAGE IS
OF POOR QUALITY

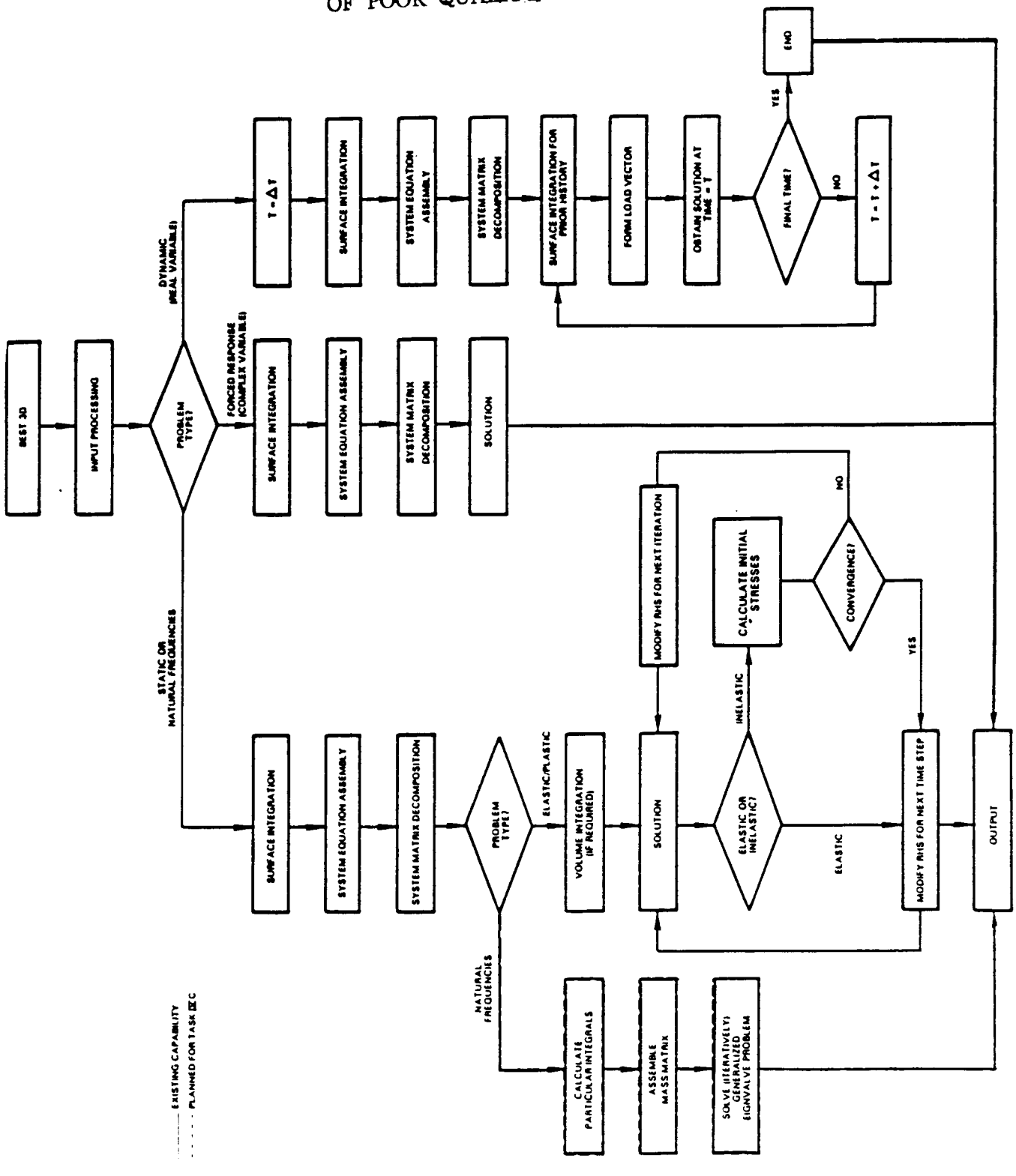

Figure 3.9: BEST3D - Overall Program Structure

3.4.3 PROGRAM INPUT

The input to BEST3D is essentially unchanged. Input formats are described in the BEST3D User's Manual (Ref. 15). The minor input changes made during Task IVC involve the addition of parameters to control the nonlinear dynamics and natural frequency calculations.

The BEST3D User's Manual (Ref. 15) is periodically updated to remain current with BEST3D development activity. The current version of the manual is consistent with the code presently available at the Lewis Research Center of the National Aeronautics and Space Administration.

3.4.4 IMPLEMENTATION OF VARIABLE STIFFNESS PLASTICITY

Equations 3.11 and 3.12 can be discretized and assembled into the following sets of equations by separating the known and unknown boundary components:

$$\begin{aligned} A^b\dot{x} &= B^b\dot{y} + C^bK\dot{\lambda} \\ \dot{u}^i &= A^i\dot{x} + B^i\dot{y} + C^iK\dot{\lambda} \\ \dot{\lambda} &= LA^\sigma\dot{x} + LB^\sigma\dot{y} + LC^\sigma K\dot{\lambda} \end{aligned} \tag{3.53}$$

where the matrices A, B, C are constant for a given problem and the matrices K, L which are dependent upon the state variable, are assumed to be constant during each small load step. The superscripts b and i denote boundary and interior related quantities, respectively.

It should be noted that the first equation is written for the boundary nodes only, the second only for the interior nodal points (excluding boundary nodes), and the third equation is written for all (boundary as well as interior) nodes likely to yield as a result of any applied loading.

The first and last of the above equations can be rewritten as:

$$A^b = \dot{b}^b + C^{\lambda b}\dot{\lambda} \tag{3.54}$$

and

$$\dot{\lambda} = A^\lambda\dot{x} + \dot{b}^\lambda + C^\lambda\dot{\lambda} \tag{3.55}$$

or

$$H\dot{\lambda} = A^\lambda\dot{x} + \dot{b}^\lambda \tag{3.56}$$

where

$$\dot{b}^b = B^b\dot{y}, C^{\lambda b} = C^bK, A^\lambda = LA^\sigma$$

$$\dot{b}^{\lambda} = LB^{\sigma}\dot{y}, C^{\lambda} = LC^{\sigma}K, H = I - C^{\lambda}$$

and I is the identity matrix.

Equation 3.55 can be recast as:

$$\dot{\lambda} = A^{0}\dot{x} + \dot{b}^{0}$$

where

$$A^{0} = H^{-1}A^{\lambda}$$
$$\dot{b}^{0} = H^{-1}b^{\lambda}$$

Substituting the above equation into 3.54 results in the final system equations:

$$A^{r}\dot{x} = \dot{b}^{r} \tag{3.57}$$

where

$$A^{r} = A^{b} - C^{\lambda b}A^{0}$$
$$b^{r} = \dot{b}^{b} - C^{\lambda}$$

The above equation can be solved to evaluate the unknown vector $\dot{x}$ at boundary nodes for every increment of loading. It should be noted that the matrix A^{b} is the reduced system matrix and $\dot{b}^{b}$ the corresponding right hand side vector of a similarly posed elastic problem. The present formulation is similar to the variable stiffness approach used in the finite element method since the system matrix on the boundary as well as the right hand side vector is modified for each increment of loading.

The solution process does not involve any iterative procedure, instead the substantial part of the solution effort is spent on assembly of the system equations for each load step. These operations can be described as follows:

1. Impose an arbitrary boundary loading and solve the elastic problem in the usual manner.
2. Scale the elastic solution such that the highest stressed nodes are at yield.
3. Apply a small load increment and compute K and L matrices using the past history.
4. Form the system equation and solve for $\dot{x}$ from

$$A^{r}\dot{x} = \dot{b}^{r}$$

5. Evaluate $\dot{\lambda}$ from

$$\dot{\lambda} = A^{0}\dot{x} + \dot{b}^{0}$$

6. Evaluate $\dot{\sigma}$ and $\dot{u}$ and accumulate the incremental quantities.

7. Return to step (3) if the displacements are less than a specified norm. Otherwise, failure is assumed to have occurred.

It is of interest to note that the matrices K, L do not exist in the elastic region, therefore, the corresponding equations involving these matrices are formed, and $\dot{\lambda}$ is determined, only for the plastic nodes.

Further, the load step must be small (usually less than five percent of yield load). When the yield condition is violated, an initial stress equilibrium correction is applied to bring back the stress point to the yield surface and this correction is taken forward to the next load step.

3.4.5 INCORPORATION OF PARTICULAR INTEGRALS

The branch designed for the incorporation of particular integrals for the solution of problems with thermal loading, inhomogeneity and/or embedded holes or cracks is shown in Figure 3.10. It is closely related to the algorithm, described in the Second Annual Status Report (NASA CR-175060), for the determination of natural frequencies. Following the calculation and storage of the coefficient matrices for both the boundary and interior stress equations, the displacements and tractions due to the particular solution are calculated. The full matrices containing the particular solution values are never stored, since the required multiplications with already existing boundary element matrices are carried out as the calculation proceeds. After the system matrix assembly the weights used in the initial strain approximation are eliminated from the system, leading to a modified system matrix similar to that used in variable stiffness plasticity. This matrix is then decomposed and the remainder of the problem solved exactly as in the original code.

3.4.6 EXTRACTION OF EIGENVALUES

The routine used for the solution of the generalized algebraic eigenvalue problem is based on the work of Ref. 16. The original paper addressed the extraction of the largest few eigenvalues of a very large, very sparse system arising in the development of multi-grid methods. Two processes, an iteration and a purification step, were used in the original method. To date, only the iterative process has been required in the BEST3D application. In order to employ the algorithm in BEST3D it was necessary to reformulate it for the generalized eigenvalue problem and adapt it to the block storage used in BEST3D.

The generalized eigenvalue problem:

$$(A - \omega^2 B)\underline{x} = 0$$

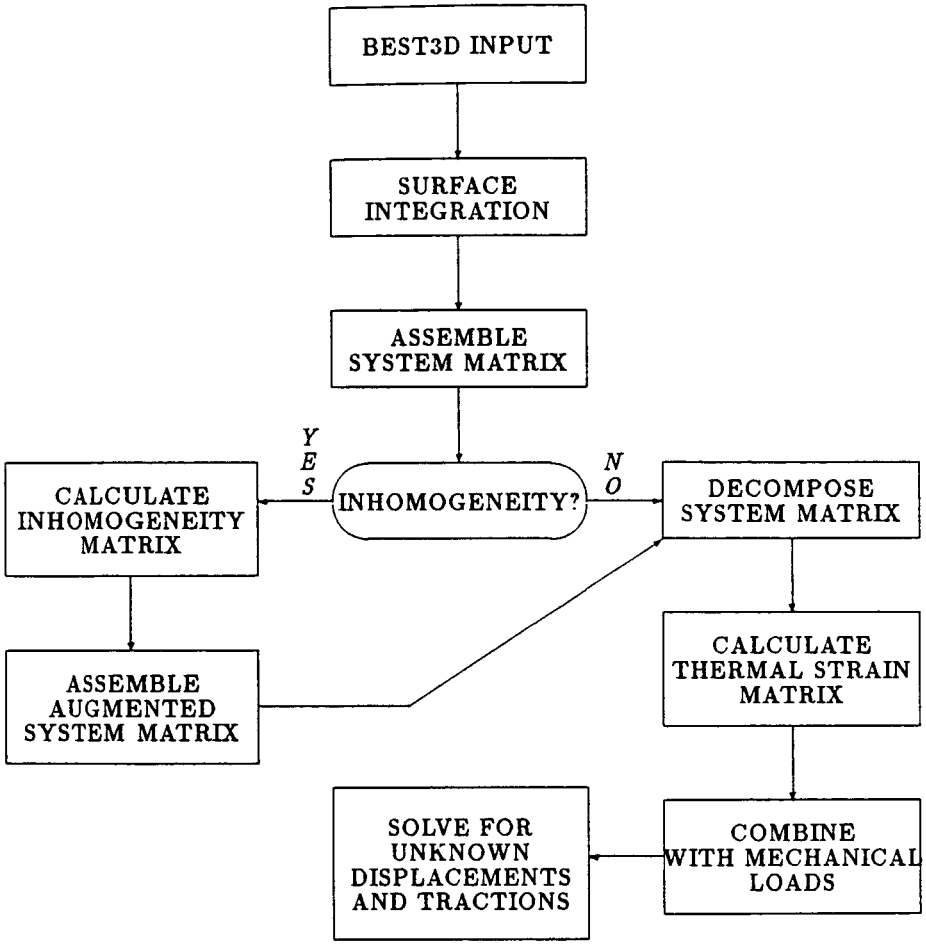

Figure 3.10: Incorporation of Particular Integrals

in which the lowest eigenvalues are sought, is reformulated as the ordinary eigenvalue problem:

$$(A^{-1}B - \lambda I)\underline{x} = 0$$

with,

$$\lambda = 1/\omega^2$$

in which the largest few eigenvalues are sought. Starting from an arbitrary initial vector, $\underline{x}^0$, successive vectors orthogonal to one another with respect to the matrix $A^{-1}B$ are formed. At each step of the iteration an upper Hessenberg matrix is formed, whose eigenvalues converge to the eigenvalues of the original system. Convergence is excellent, with the first mode usually obtained in five to eight iterations. Computational experience has shown that one additional mode per iteration is normally obtained thereafter.

3.4.7 NONLINEAR DYNAMICS

Equations (3.50) and (3.51) provide the formal basis for developing the dynamic plasticity algorithm. However, the initial stresses $\Delta\sigma^0_{ij}$ defined in equations (3.50) and (3.51) are not known *a priori* and have to be determined by satisfying the constitutive relations. Thus, equations (3.50) and (3.51) and (3.52) can be regarded as a coupled system of nonlinear equations. In the present implementation, equation (3.51) and (3.52) are used to calculate the stresses at interior and boundary points and the nonlinear material model is then used to evaluate the inelastic stresses. Since the volume integrals of inelastic stress vanish except in regions of nonlinear material response, approximations of geometry and field quantities are required only where nonlinearity is expected. In the present work, isoparametric (quadratic) volume cells are used for approximating the geometry and the variation of initial stresses such that:

$$\begin{aligned} x_i &= M_\beta(\underline{\eta})\bar{x}_{i\beta} \\ \sigma^0_{ij} &= M_\beta(\underline{\eta})\bar{\sigma}^0_{ij\beta} \end{aligned} \tag{3.58}$$

where x_i are cartesian coordinates, $\bar{x}_{i\beta}$ are nodal coordinates of the volume cell, M_β ($\beta = 1, 20$) are the quadratic shape functions for the volume cell, and the overbar denotes nodal quantities.

The volume integral of equation (3.50) can then be represented as:

$$\begin{aligned} &\int_0^T \int_V B_{ilk}(\underline{x}, T; \underline{\xi}^b, \tau)\, \Delta\sigma^0_{il}(\underline{x}, \tau)\, dV\, d\tau = \\ &\quad \sum_{m=1}^{L} \int_0^T \int_{V_m} B_{ilj}(\underline{x}^m(\underline{\eta}), T; \underline{\xi}^b, \tau)\, M_\beta(\underline{\eta})\, dV_m\, \Delta\bar{\sigma}^{0m}_{il\beta}\, d\tau \end{aligned} \tag{3.59}$$

where:

- $\underline{\xi}^b$ is the field point on the boundary (boundary node),
- $\underline{x}^m(\underline{\eta})$ is a point in cell m,
- $\Delta\bar{\sigma}^{0m}_{il\beta}$ are the nodal values of incremental initial stress for the m^{th} cell,
- V_m is the m^{th} volume cell, and
- L is the total number of cells in a single region.

Similarly, the volume integral of the interior stress equation (3.51) can be expressed as:

$$\int_0^T \int_V B^\sigma_{iljk}(\underline{x}, T; \underline{\xi}, \tau)\, \Delta\sigma^0_{il}(\underline{x}, \tau)\, dV\, d\tau = \tag{3.60}$$

$$\sum_{m=1}^{L} \int_0^T \int_{V_m} B^{\sigma}_{iljk}(\underline{x}^m(\eta), T; \underline{\xi}, \tau)\ M_\beta(\underline{\eta})\ dV_m\ \Delta\bar{\sigma}^{0m}_{il\beta}\ d\tau$$

in which the time integral is treated analytically as before.

The volume integration scheme used in this work is substantially similar to the quasi-static nonlinear analysis except that the cells are sub-divided to account for the silent part of the cell which has not yet been affected by the shear and pressure waves.

3.4.7.1 TIME-STEPPING In order to obtain the nonlinear transient response at a time T_n, the time axis is discretized into N equal time intervals, i.e.

$$T_N = \sum_{n=1}^{N} n\Delta T$$

where ΔT is the time step.

Using equation (3.4.7.1), the integral equation (3.50) can be written as:

$$c_{ij}\Delta u_i(\underline{\xi}, T_N) - \int_{T_{N-1}}^{T_N} \int_S (G_{ij}\Delta t_i - F_{ij}\Delta u_i)\ dS\ d\tau$$

$$-\int_{T_{N-1}}^{T_N} \int_V B_{ilj}\Delta\sigma^0_{il}\ dV\ d\tau \ = \tag{3.61}$$

$$\int_{\tau=0}^{T_{N-1}} \int_S (G_{ij}\Delta t_i - F_{ij}\Delta u_i) dS d\tau + \int_{\tau=0}^{T_{N-1}} B_{ilj}\Delta\sigma^0_{il} dV d\tau$$

For the present case the linear time interpolation scheme is used to approximate the time variation of the field quantities during a time step because the same scheme can also be used for constant time interpolation with averaging.

After the usual discretization and integrations (in time and space), the integral equations (3.61) are transformed into an assembled system equation of the form:

$$\begin{aligned}
&[A_2^1][\Delta X^N] - [B_2^1][\Delta Y^N] - [C_2^1][\Delta\sigma^{0,N}] \\
&= -\sum_{n=2}^{N} \Big[[A_2^n + A_1^{n-1}][\Delta X^{N-n+1}] - [B_2^n + B_1^{n-1}][\Delta Y^{N-n+1}] \\
&\quad + [C_2^n + C_1^{n-1}][\Delta\sigma^{0,N-n+1}]\Big]
\end{aligned} \tag{3.62}$$

or

$$[A_2^1][\Delta X^N] = [B_2^1][\Delta Y^N] + [C_2^1][\Delta\sigma^{0,N}] + [R^N] \tag{3.63}$$

or

$$A^b \Delta X^N = \Delta b^{bN} + \Delta b^{0,bn} \tag{3.64}$$

where:

- A and B are the matrices related to the unknown and known incremental displacements and tractions;
- C is the matrix related to the initial stresses;
- ΔX and ΔY are the vectors of unknown and known incremental displacements and tractions;
- for $\Delta X, \Delta Y$ and $\Delta\sigma^0$, superscripts denote time, i.e., $\Delta X^n = X^n - X^{n-1}$;
- for the A, B and C matrices, superscripts denote the time step when they are calculated, and subscripts denote the local time node (1 or 2);
- R^N is the effect of past dynamic history;
- and,

$$\Delta b^{bN} = [B_2^1][\Delta Y^N] + [R^N]$$
$$A^b = [A_2^1]$$
$$\Delta b^{0,bN} = [D_2^1][\Delta\sigma^{0,N}]$$

Similarly, the integral equation for stresses can be written in a discretized form as:

$$[\Delta\sigma^N] = [\bar{A}_2^1][\Delta X^N] + [\bar{B}_2^1][\Delta Y^N] + [\bar{C}_2^1][\Delta\sigma^{0,N}] + [R^{\sigma N}] \tag{3.65}$$

or

$$\Delta\sigma^N = A^\sigma \Delta X^N + \Delta b^{\sigma N} + \Delta b^{0,\sigma N} \tag{3.66}$$

where the overbar indicates that the matrices are related to the stress equation:

$$A^\sigma = [\bar{A}_2^1]; \quad \Delta\sigma^N = [\bar{B}_2^1][\Delta Y^N] + [R^{\sigma N}]$$

and;

$$\Delta b^{0,\sigma N} = [\bar{C}_2^1][\Delta\sigma^{0,N}]$$

3.4.7.2 ITERATIVE SOLUTION ALGORITHM FOR DYNAMIC PLASTICITY The algorithm described here provides the solution of system equations (3.62) and (3.65). The solution of these system equations requires complete knowledge of the initial stress distribution within the yielded region that is induced by the imposition of the current increment of boundary loading. This, unfortunately, is not known *a priori* for a particular load increment and, therefore, an iteratve process must be employed within each time step.

This incremental algorithm can be described as follows:

1. Obtain the transient elastic solution for an arbitrary increment of boundary loading ΔY^N during the time interval T_{n-1} to T_n, as

$$A^b \Delta X^N = \Delta b^{bN}$$

and

$$\Delta \sigma^N = A^\sigma \Delta X^N + \Delta b^{\sigma N}$$

where N is the time step number. If the material has not yet yielded, accumulate X-vectors, i.e., $X^N = X^{N-1} + \Delta X^N$.

2. If the material has previously yielded, go to step (6).

3. Check whether any node has yielded during the current time step. If the material has not yielded yet, accumulate stress and strain, and go back to step (1).

4. Calculate the value of σ^0, the equivalent stress, by using $\sigma^T = \sigma^{N-1} + \Delta\sigma^N$ as the stress changes and compile a list of yielded nodes. For elastic nodes accumulate the stress and strain, i.e., $\sigma^n = \sigma^T$ and $\epsilon^N = \epsilon^{N-1} + [D^e]^{-1}\Delta\sigma^N$. Calculate the correct stress at the elastoplastic nodes by using the elastoplastic stress-strain relations $\Delta\sigma^{ep} = D^{ep}\Delta\epsilon$ and using the elastic strain increments as a first approximation. Modify the stress history for yielded cells $\sigma^N = \sigma N - 1 + \Delta\sigma^{ep}$. Calculate initial stress, $\Delta\sigma^0 = \sigma^T - \sigma^N$.

5. Assume $\Delta b^{\sigma N} = 0$ and $\Delta b^{bN} = 0$ and, using the generated initial stress $\Delta\sigma^0$, calculate a new $\Delta\bar{X}^N$ by using equation (3.64) and $\Delta\sigma^N$ by using equation (3.66). Calculate the equivalent stresses by using the history $\sigma^T = \sigma^N + \Delta\sigma^N$ and compile a list of yielded nodes. For elastic nodes, accumulate the stress, $\sigma^N = \sigma^T$, and strain. For the elasto-plastic nodes calculate the current stress increment, $\Delta\sigma^{ep}$. The initial stresses generated are $\Delta\sigma^0 = \Delta\sigma^N - \Delta\sigma^{ep}$. Modify the stress history for the yielded nodes, $\sigma^N = \sigma^N + \Delta^{ep}$. Accumulate ΔX^N and $\Delta\sigma^{0,N}$ (i.e.= $\Delta X^N = \Delta X^N + \Delta\bar{X}^N$ and $\Delta\sigma^{0N} = \Delta\sigma^{0N} + \Delta\sigma^0$) so that they can be used in the next time step for past convolution.

6. Check if the initial stresses $\Delta\sigma^0$ are less than an acceptable norm. If so, go to step (1). If not, go back to step (5). If the number of iterations exceeds a fixed number (usually 50), it is assumed that collapse has occurred.

3.5 VALIDATION/VERIFICATION

3.5.1 SUMMARY

During Task IVC, significant new capabilities were added to BEST3D. In addition, new algorithms presently under development were tested using two-dimensional programs or special purpose three-dimensional codes. The validation and verification of these new capabilities and the continuing general verification of the BEST3D code are discussed in the subsections which follow. Attention in this report is directed primarily to the dynamic capabilities of BEST3D, the initial evaluation of variable stiffness plasticity and the new particular integral formulations and the continuing application of BEST3D to three-dimensional component analysis.

Table 3.1: Calibration of Major BEST3D Capabilities

BEST3D CAPABILITY	RESULTS USED		
	EXACT	OTHER NUMERICAL	EXPERIMENTAL
ELASTICITY			
general capabilities	X		
stress concentrations	X	X	Benchmark Notch Diffuser Case Boss
thermal stress	X		
PLASTICITY			
general capabilities	X	Finite Element Alternate BEM Algorithms	
structural details	X	Finite Element Analyses for Experimental Programs	Theocaris /Marketos Benchmark Notch
thermoplasticity	X		Carmen/Hess
DYNAMICS			
time domain	X	Pao/Mow	
frequency domain	X		Woods
EIGENVALUES	X	X	Keilb, *et. al.*

The major capabilities of BEST3D together with analytical and/or experimental used to calibrate the capabilities are summarized in Table 3.1.

3.5.2 MULTI-REGION INTERFACES

One of the key features of the BEST3D code is the ability to join two subregions across one or more interface elements, with either complete fixity or tangential sliding allowed at the interface. This capability is a key to the successful modelling of complex geometry and of the interaction between parts such as blades and disks. In order to verify this capability in BEST3D, a highly idealized model of one-half of a compressor dovetail was built. The model, shown in Figure 3.11, consists of twenty eight quadratic elements. The model was held on rollers and loaded with a radial load on the simulated blade, with centrifugal load and with combined centrifugal and radial loads. Cases were run with both fixed and sliding interface conditions.

In order to check the correct operation of the BEST3D code for these problems, for which no analytical solutions are available, cases were run in which the modulus of the simulated disk (Region 1) was set to be several orders of magnitude larger than that in the simulated attachment (Region 2). In such cases the response in the attachment is the same as that obtained when the attachment alone is run with either fixed or sliding contact on the interface.

For all of the cases run, the results of the single region analysis agreed with the two region, multi-material analysis.

3.5.3 PLASTICITY USING VARIABLE STIFFNESS ALGORITHM

The accuracy and efficiency of the newly incorporated variable stiffness plasticity algorithm in BEST3D has been investigated using the problem of the radial expansion of a thick, internally pressurized cylinder. The ratio of outer to inner radius of the cylinder is 2.0. The material has a Young's modulus of 2600, Poisson's ratio of 0.3 and a yield stress of 600. The piecewise linear approximation to the stress-strain curve is shown in Figure 3.12. The BEST3D model consisted of eighteen boundary elements and four (twenty node) volume cells.

Three analyses were run:

1. iterative algorithm with load increments of 5 percent of the yield load for the first seven increments, with 2 percent load increments thereafter;

2. variable stiffness algorithm with 2 percent load increments throughout;

3. variable stiffness algorithm with load increments identical to those used for the iterative algorithm.

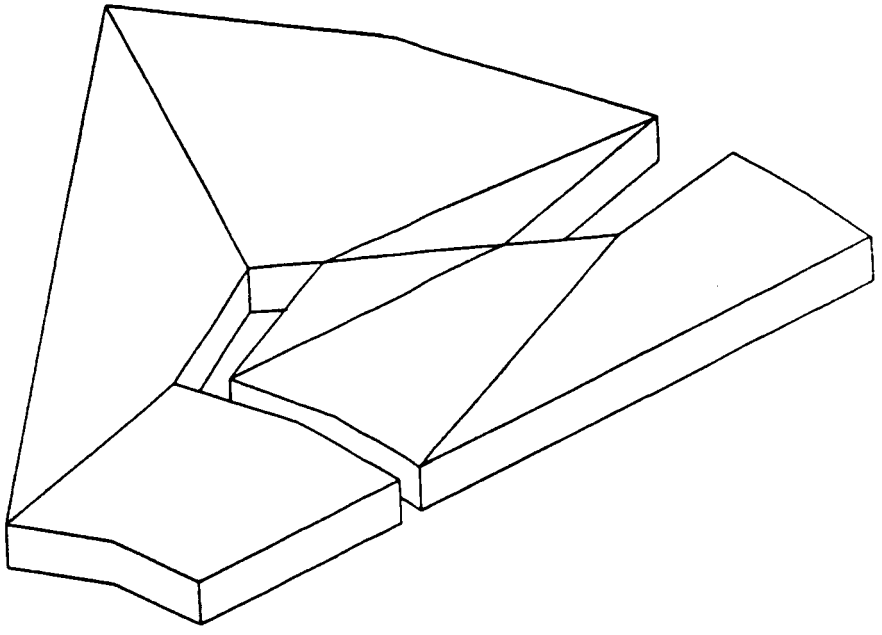

Figure 3.11: Simulated Disk/Attachment BEST3D Model

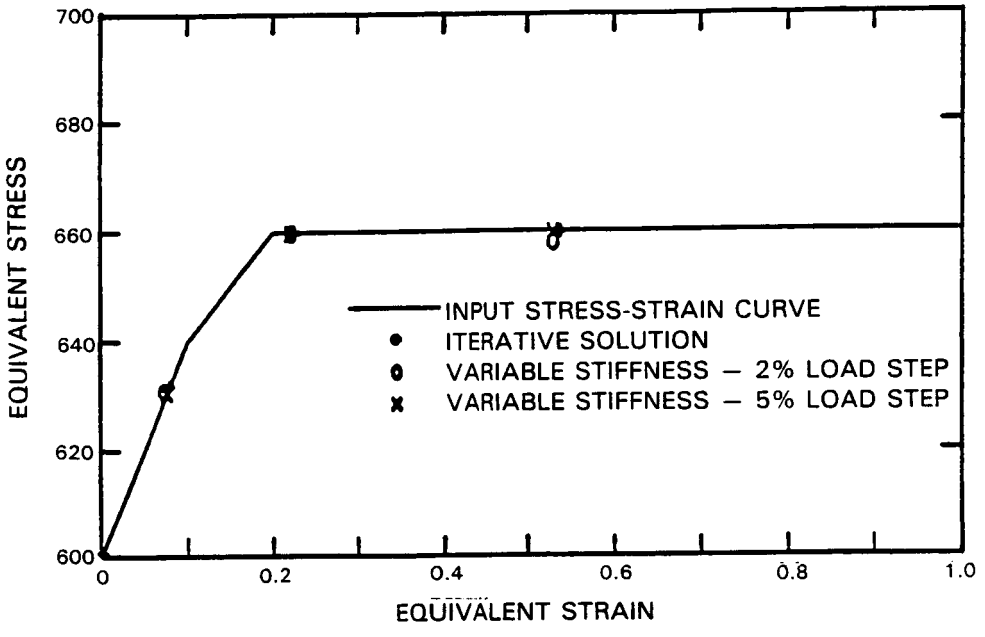

Figure 3.12: Stress-Strain Response

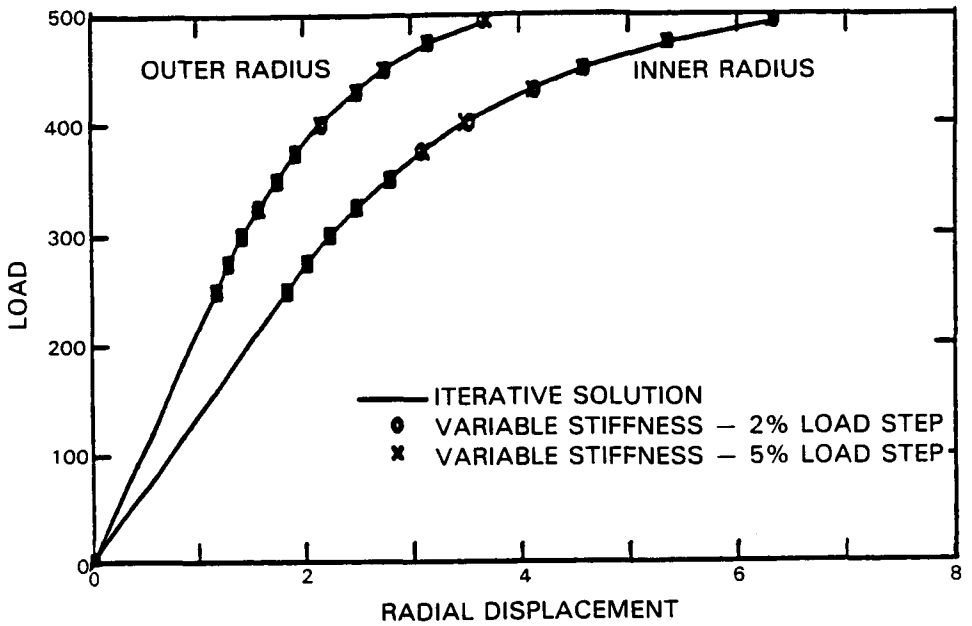

Figure 3.13: Load - Displacement Response

All three analyses gave virtually identical load-displacement curves, at both the inner and outer radii (Figure 3.13). Further, there is excellent agreement in the stress variation through the thickness of the cylinder (Figure 3.14), and in the tracking of the stress-strain curve (Figure 3.12).

The run time for the third (variable stiffness) analysis (on the SUNY-B HP9000) was 1.6 times that required for the iterative analysis (analysis 1). The current results indicate the possibility, presently being investigated, of using even larger load increments for the variable stiffness analysis. This would lead to considerable reductions in computing time, since variable stiffness computing time is directly proportional to the number of load increments. Further, very significant opportunities exist for improving the efficiency of the variable stiffness algorithm, as compared to the iterative algorithm, which is already the product of ten years of development.

3.5.4 THERMAL/INELASTIC ANALYSIS USING PARTICULAR INTEGRALS

The major limitation in use of the boundary element method as a general purpose analysis tool is that a volume discretization and integration must be introduced to account for inelastic response, elastic inhomogeneity and/or non-steady state thermal strains. This

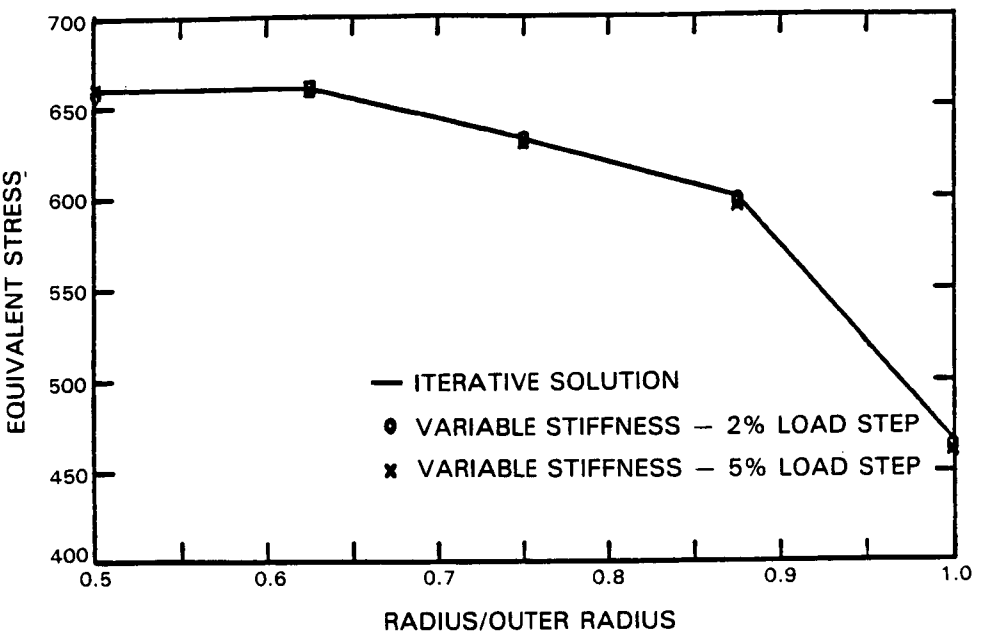

Figure 3.14: Stress Variation through Thickness of Cylinder

requirement for volume discretization meant that the boundary element method became less attractive relative to the finite element method, in which inhomogeneity and thermal strains can be incorporated within the same framework as homogeneous elastic analysis.

A high priority in the current phase of the inelastic methods program has been the reduction (or, preferably, elimination) of volume integration requirements. An improved analytical formulation has been gradually developed, starting from the exact initial strain solution for a cuboid and the development of particular integrals for centrifugal loads. The development of a formulation allowing solution of thermal stress problems and of problems involving smoothly varying elastic inhomogeneity (such as that caused by the variation of Young's modulus with temperature) has now been completed.

In order to evaluate the potential benefits of this new approach the simplest case, the particular integral for thermal strains, has been incorporated in BEST3D. Since thermal stress capability using volume integration is already provided in BEST3D, direct comparison is possible between the new and old algorithms. The test problem shown in Figure 3.15, is geometrically simple, but very difficult to solve accurately. The difficulty arises from the fact that all the loading in the problem is generated by volume integration, since there are no mechanical loads applied. As a result the solution is very sensitive to volume discretization (especially cell aspect ratios) and to volume integration accuracy. In this analysis the cylinder is allowed to grow on rollers in response to a uniform tem-

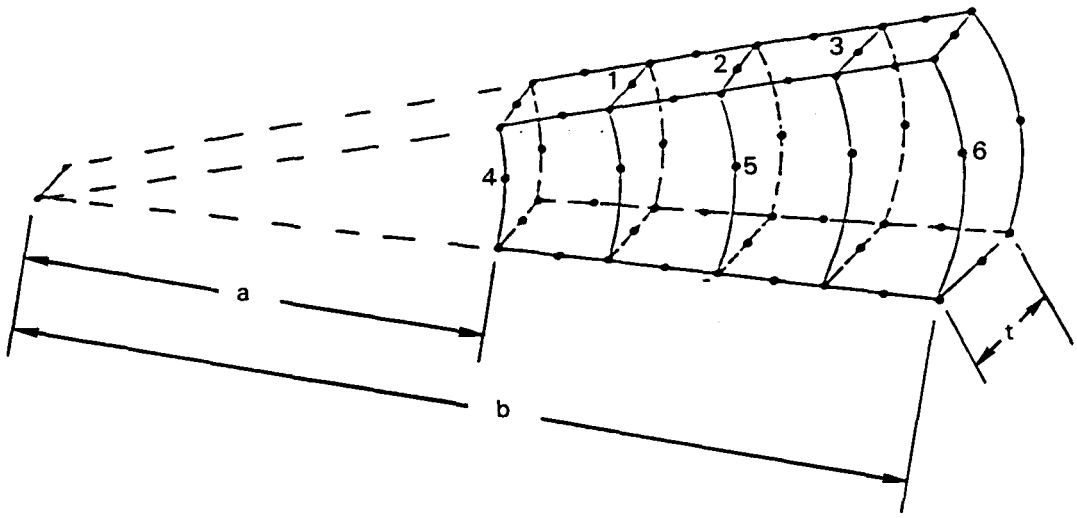

a = 10 b = 20

t = 0.5 CASE 1

t = 0.1 CASE 2

α = 0.01 E = 2600.0 ΔT = +100.0

ν = 0.3

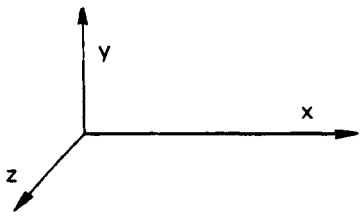

THERMAL STRESS = $\frac{\alpha E(\Delta T)}{(1-2\nu)}$ = 6500.0

ANALYTIC SOLUTION, PLANE STRESS CONDITIONS

RADIAL DISPLACEMENT $u_r = \alpha(\Delta T)r$, r = RADIAL DISTANCE

STRESS $\sigma_{ij} = 0.0$

Figure 3.15: Boundary Element Model of a Thin Disk

perature increase. The analytical solution to this problem is a linear variation of radial displacement with radius and a zero stress state. Two cases were analyzed. In the first the disk thickness was .5 inch and in the second it was 0.1 inch. These cases produce cell aspect ratios of 5:1 and 25:1, respectively. The results are summarized in Tables 3.2 and 3.3.

It can be seen that the particular integral approach, for both cases, produces much more accurate results than the volume integral approach. Even in the most demanding case, the worst errors are .2% in displacement and 1.2% in stress (relative to $E\alpha(\Delta T)/(1-2\nu)$).

Table 3.2: Free Thermal Expansion of a Thin Disk — $(b-a)/t = 20$

	Type of Analysis	Nodes					
		1	2	3	4	5	6
u_r	Volume Integration	-	-	-	9.41	14.272	18.872
	Particular Integrals	-	-	-	9.99	14.98	19.980
	Analytical Solution	-	-	-	10.0	15.0	20.0
σ_{yy}	Volume Integration	983.8	1113.5	1119.2	218.9	-177.8	-346.9
	Particular Integrals	1.6	6.1	3.1	-5.9	0.7	-5.4

Table 3.3: Free Thermal Expansion of a Thin Disk — $(b-a)/t = 100$

	Type of Analysis	Nodes					
		1	2	3	4	5	6
u_r	Volume Integration	-	-	-	8.6	11.5	14.2
	Particular Integrals	-	-	-	9.972	14.964	19.946
	Analytic Solution	-	-	-	10.0	15.0	20.0
σ_{yy}	Volume Integration	259.1	405.5	532.2	-1104.9	-1034.1	-1494.6
	Particular Integrals	-75.9	-70.9	-74.4	-10.5	-5.9	-18.8

Recently the problem of the inelastic expansion of a thick cylinder described in Section 3.5.3 was analyzed by this newly developed method. The results were virtually indistinguishable from the iterative plasticity results already shown in Figures 3.12 through 3.14.

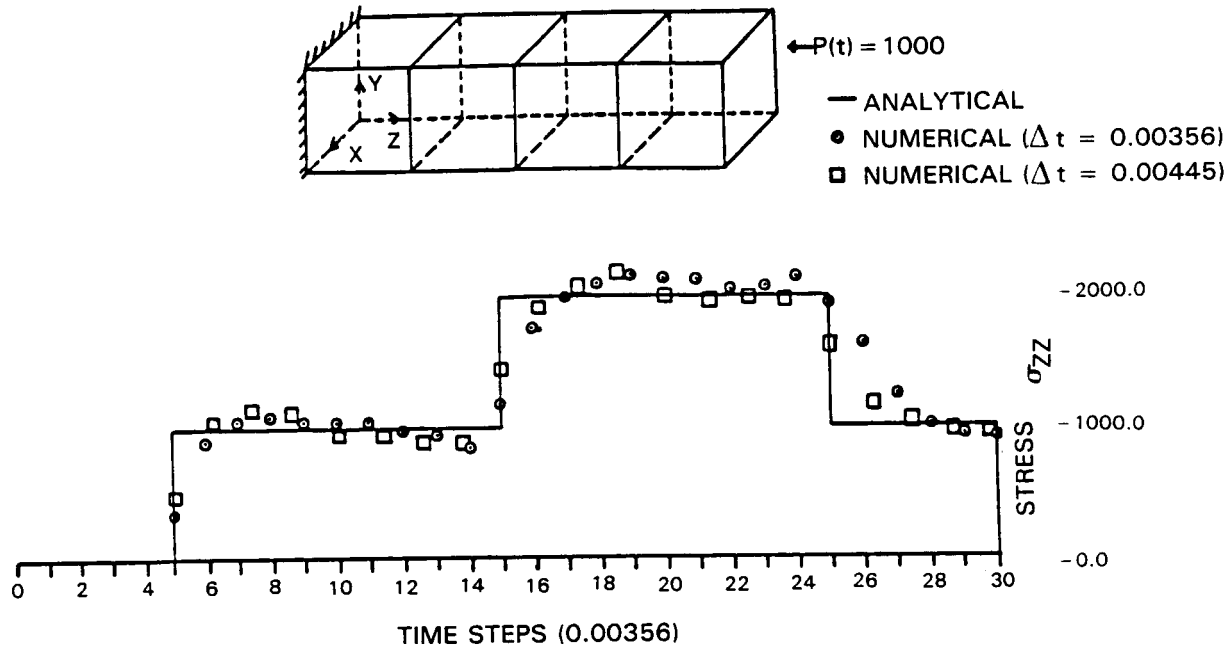

Figure 3.16: Dynamic Stress in Square Cantilever under End Load

3.5.5 BAR SUBJECTED TO TRANSIENT END LOAD

1. Square cross-section:

A bar with square cross-section is held along its sides by lubricated rollers and is fixed at one end. The free end is subjected to a suddenly applied and maintained uniform compression $t_z = 1000$. The dimensions of the bar are $L = 8.0$ and $b = 2.0$. In view of the material properties, the characteristic time required for the compressive wave to reach the fixed end is 0.0578 sec. Figure 3.16 shows the discretization and the numerical results for the normal stress, in which the results from the time domain algorithm for two different time steps ΔT are compared with the exact analytical solution for one-dimensional stress wave propagation. Although the numerical results are in good agreement with the analytical solution, it is clearly very difficult to reproduce the sharp jump in the stress as the disturbance reaches the point initially and when the reflected stress wave returns to the same location. This difficulty has been observed elsewhere as well.

The axial displacement history at the free end is shown in Figure 3.17. The displacements are normalized by static displacements and the time is normalized with respect to the characteristic time required for the compressive wave to reach the fixed end. It can be seen that the numerical results are in good agreement with the analytical solution. The

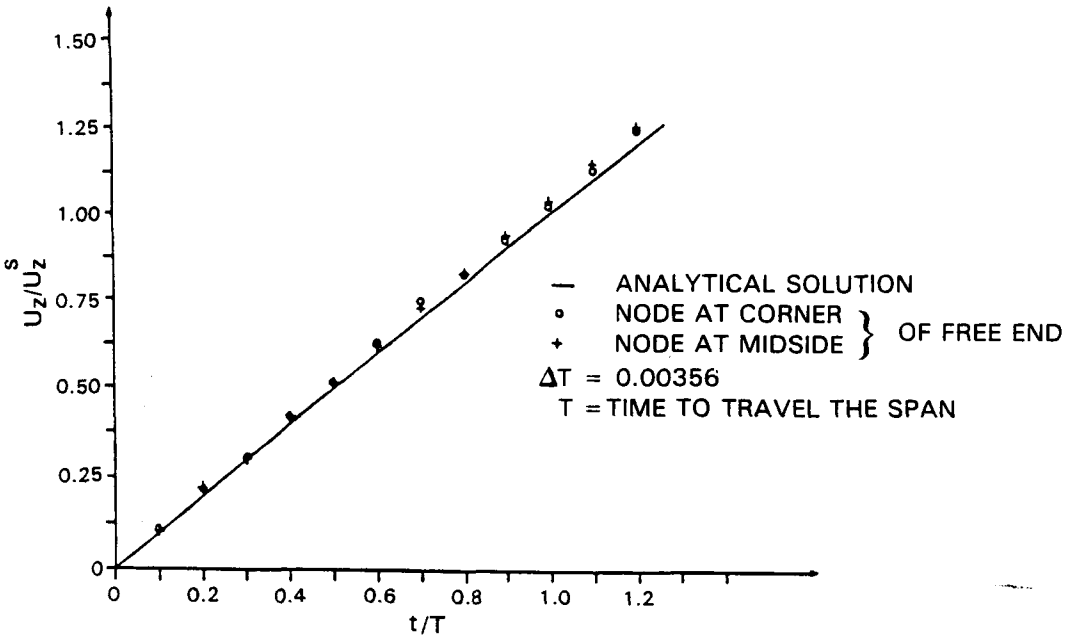

Figure 3.17: Deflection at Free End of Square Cantilever

differences are mainly due to the three-dimensional nature of the simulated problem.

2. Circular-cross-section:

In order to investigate the effects of the cross-section on the numerical results, a bar with circular cross-section having the same material properties and boundary conditions as described in the last example was analyzed. The boundary element mesh for this problem is shown in Figure 3.18. The bar has a length $L = 5$ and diameter $d = 1$. Thus, the characteristic time required for the compressive wave to reach the fixed end is 0.02236 sec. The time step used in this example is $\Delta T = 0.004475$ sec.

Figure 3.19 shows the numerical results for the normal stress at the midspan of the bar compared with a one-dimensional analytical solution. As mentioned in the last example, the sharp jumps in stress are diffused in the numerical results. However, by using more elements and smaller time steps, the numerical results in the vicinity of the jumps will agree more closely with the analytical solution.

The time history of the normalized, axial displacements at the free end is plotted in Figure 3.20 against the one-dimensional analytical solution. The results are in good agreement, except for the peak displacements. The numerical peak values are less than than of the analytical solution and this results in an increase in the difference between the two solutions at later times. The difference, once again, is mainly due to the three-

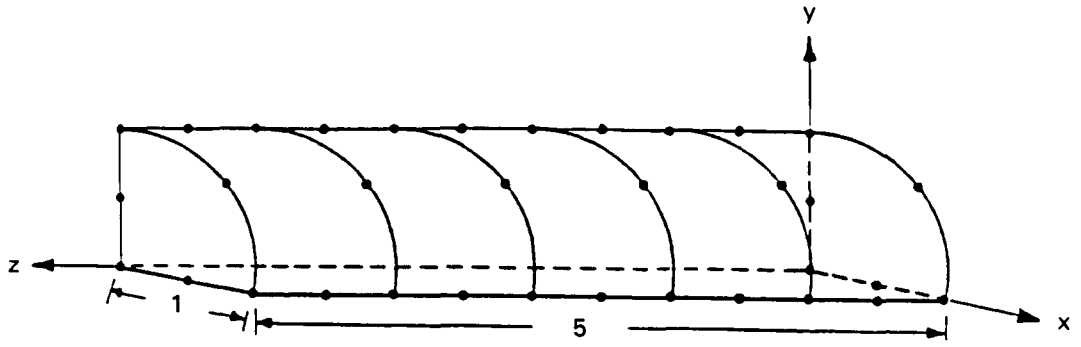

Figure 3.18: Surface Discretization of a Circular Bar

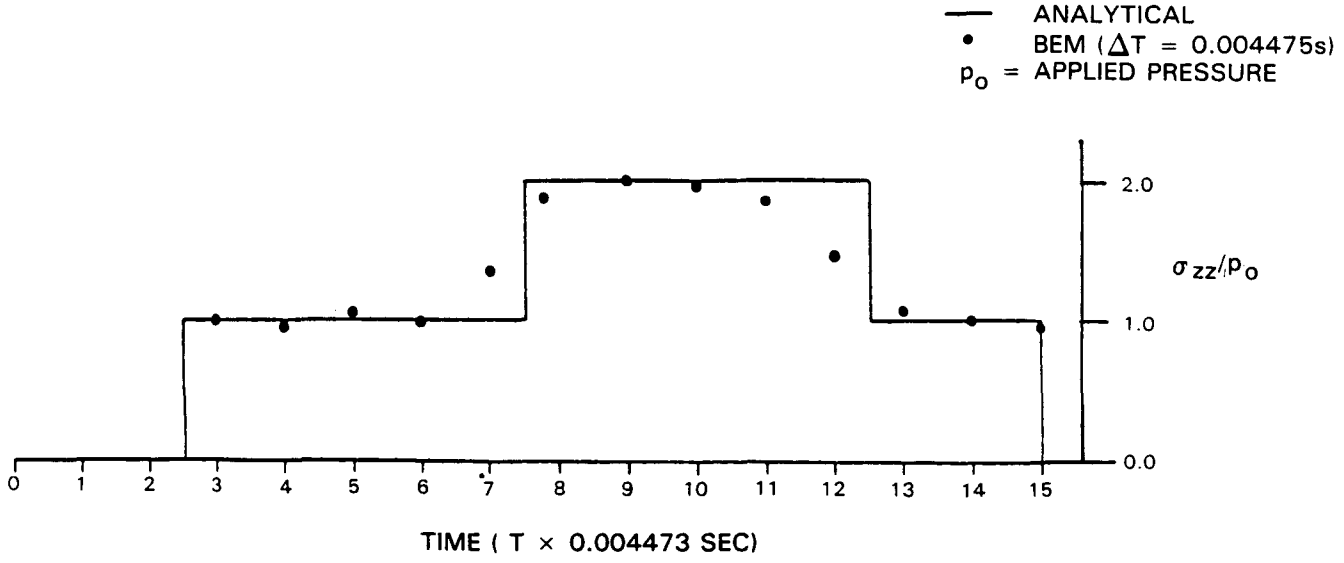

Figure 3.19: Axial Stress at Midspan of Circular Bar

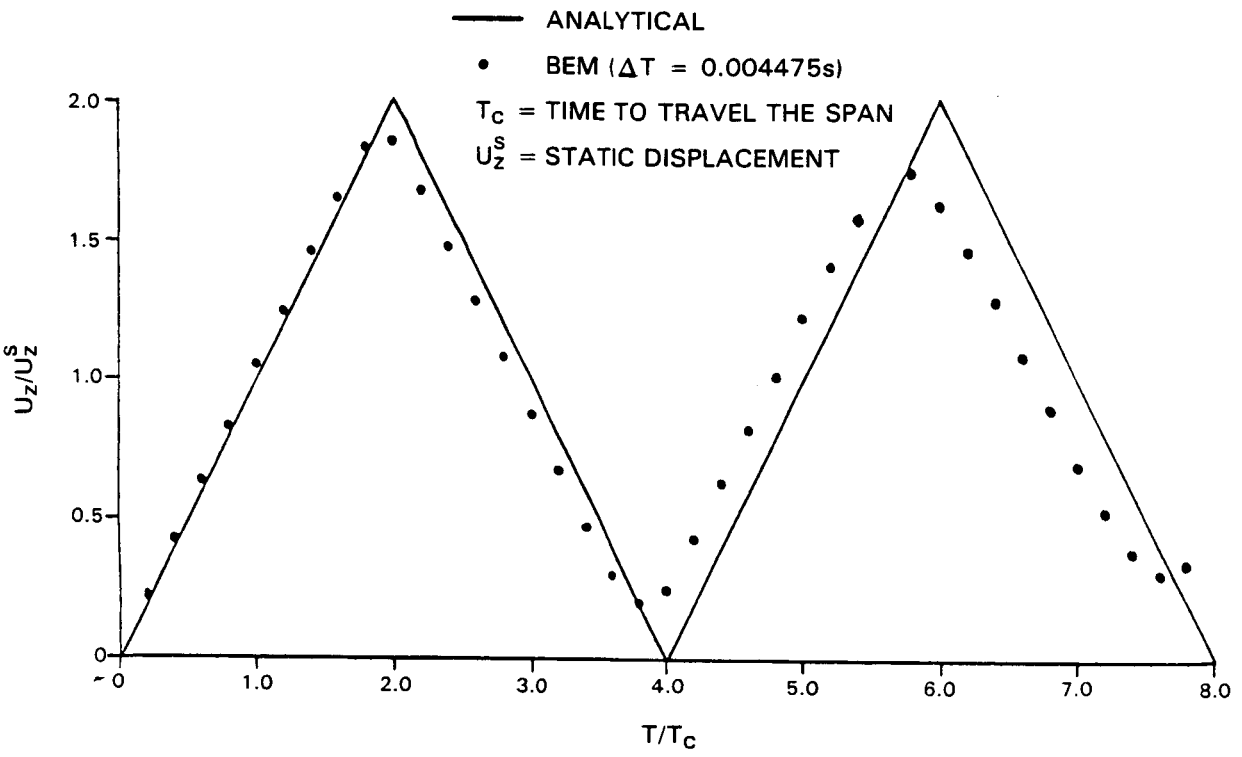

Figure 3.20: Axial Displacement at Free End of Circular Bar

dimensional nature of the problem under consideration.

3.5.6 SPHERICAL CAVITY SUBJECTED TO DYNAMIC PRESSURE

A spherical cavity is embedded in an infinite medium with $E = 8.993\text{x}10^{-6}, \nu = 0.25$, and $\rho = 2.5\text{x}10^{-4}$. The radius of the cavity is $R = 212$. Using the built-in symmetry capabilities, this problem is modeled by one octant only. The single octant modelled is idealized using three quadratic surface patches. The characteristic times required for the pressure and shear waves to travel a cavity radius are 0.00102 sec and 0.00277 sec, respectively. Four cases are considered:

1. Spherical cavity under sudden radial expansion

   A radial pressure $p = 1000$ is suddenly applied and maintained at the cavity surface. Figure 3.21 shows the time variation of deviatoric stress at the cavity surface obtained by the time domain algorithm. Concurrently plotted is the result reported by Hopkins (Ref. 27) based on the work of Hunter (Ref. 28). In general, the numerical results are in good agreement with the analytical solution. The transient, time-domain solution remains stable and reaches the expected static solution at

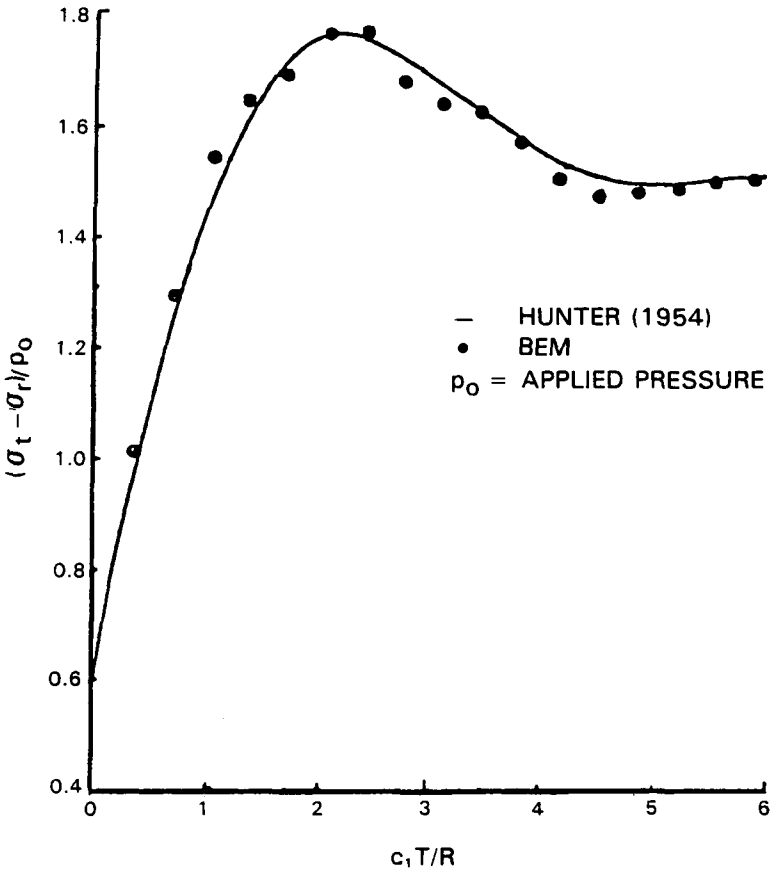

Figure 3.21: Deviatoric Stress at the Cavity Surface

larger times. It can be seen that the maximum deviatoric stress for the transient case is 1.77 times the applied pressure, whereas for the static case it is 1.54 times the applied pressure.

2. Spherical cavity subjected to a triangular pulse of radial pressure

   A triangular pulse of radial pressure, as shown in Figure 3.22, is applied at the cavity surface. This example is solved by using linear time interpolation functions and two different time steps. The radial displacements at the cavity surface are plotted in Figure 3.22. The numerical results from both the time steps are almost identical. Thus, this example once again demonstrates the stability of the present algorithm.

3. Spherical cavity subjected to a rectangular pulse of radial pressure

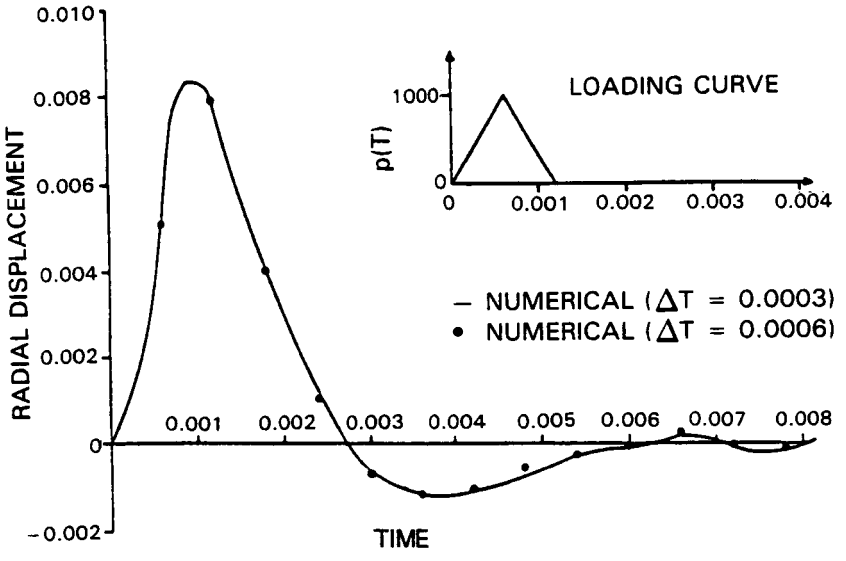

Figure 3.22: Radial Expansion of Cavity under Triangular Pulse

A rectangular pulse of radial pressure, as shown in Figure 3.23, is applied at the cavity surface. This example is also solved by using linear time interpolation functions and two different time increments. Figure 3.23 shows the time history of the radial displacement of the cavity. By comparing these results with those due to a triangular pulse (i.e. Figure 3.22), it can be seen that, in general, displacements at any time interval due to the rectangular pulse are twice that due to the triangular pulse. This is because the response depends upon the total impulse, and the total impulse due to the rectangular pulse is double that due to the triangular one. Hence, the displacement amplitude response due to the rectangular pulse is also approximately double that of the triangular pulse.

4. Spherical cavity engulfed by a pressure wave

A propagating plane pressure wave whose front is perpendicular to the z-axis (Figure 3.24) first impinges on the pole with coordinates (0,0,212). The resulting non-zero incident stresses are $\sigma^i_{zz} = -1000$, $\sigma^i_{yy} = \sigma^i_{xx} = (v/(1-v))\sigma^i_{zz}$. This wave propagation type of problem has been solved by superposition (Miklowitz, Ref. 29). A mesh using three quadrilaterals per octant (Figure 3.25) is employed here in conjunction with the time-domain approach. Figure 3.26 plots the hoop stresses $\sigma^*_{\phi\phi}$ and $\sigma^*_{\theta\theta}$ normalized by the magnitude of the incident stress σ^i_{zz} versus the non-dimensional time $\tau^* = RT/c$.

The plots are for three locations on the surface of the cavity: the two poles ($\phi = 0, \pi$)

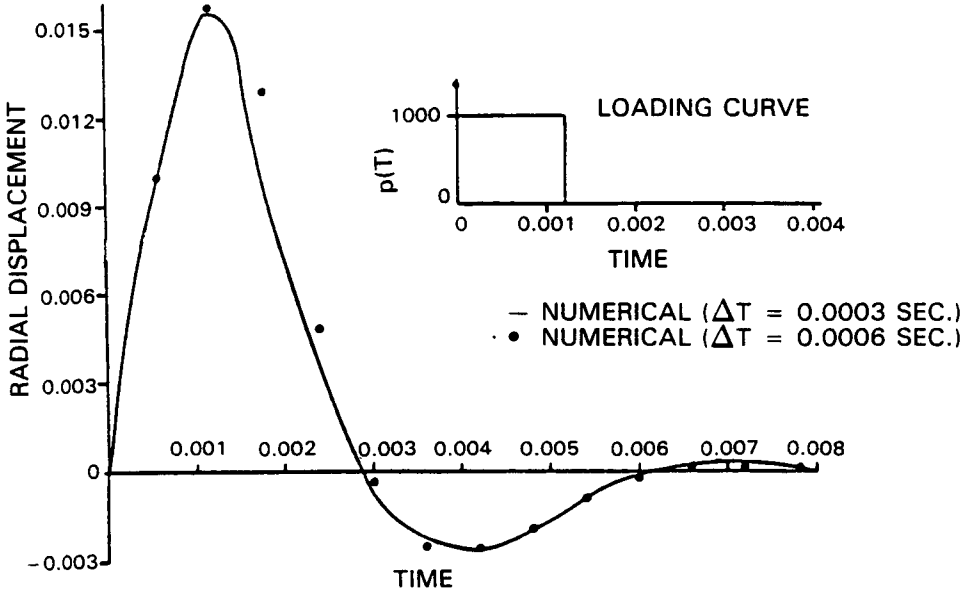

Figure 3.23: Radial Expansion of Cavity under Rectangular Pulse

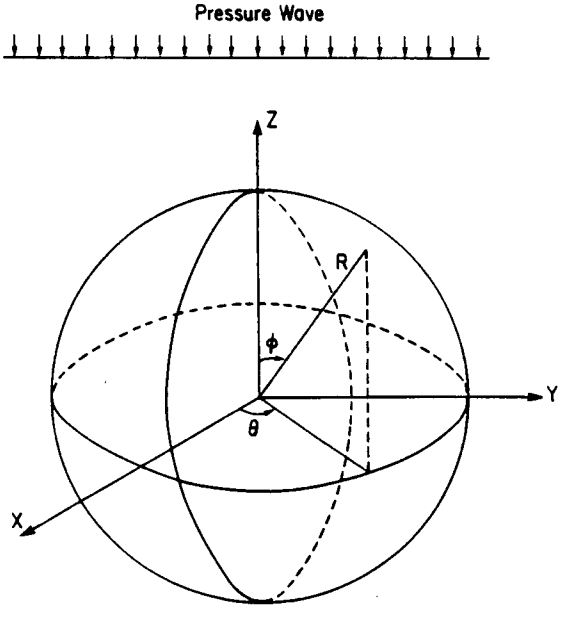

Figure 3.24: Spherical Cavity Engulfed by a Pressure Wave

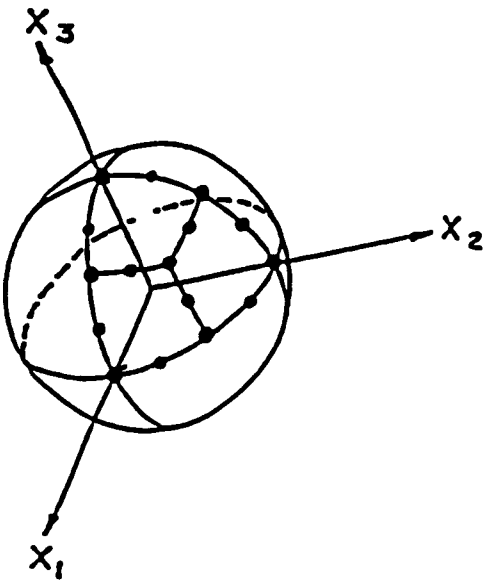

Figure 3.25: Mesh Used for the Analysis of Spherical Cavity

and the equator ($\phi = \pi/2$). Concurrently plotted are the results (Pao and Mow, Ref. 30; Norwood and Miklowitz, Ref. 31), obtained by analytical inversion of the Fourier transformed solution. Good agreement is observed between the two solutions. Finally, Figure 3.27 plots the radial displacement time history at the same three locations.

3.5.7 DYNAMIC LOADING ON A SQUARE FOOTING ON A HALF SPACE

In this example, a square flexible footing on a half-space (the soil under the footing) is subjected to time dependent vertical tractions. The mesh for this problem is shown in Figure 3.28(a). The side of the footing is $B = 2b = 2$, and the material properties of the half-space in any consistent units are: elastic modulus $E = 2.6$, Poisson's ratio $= 0.3$ and mass density $= 1.0$.

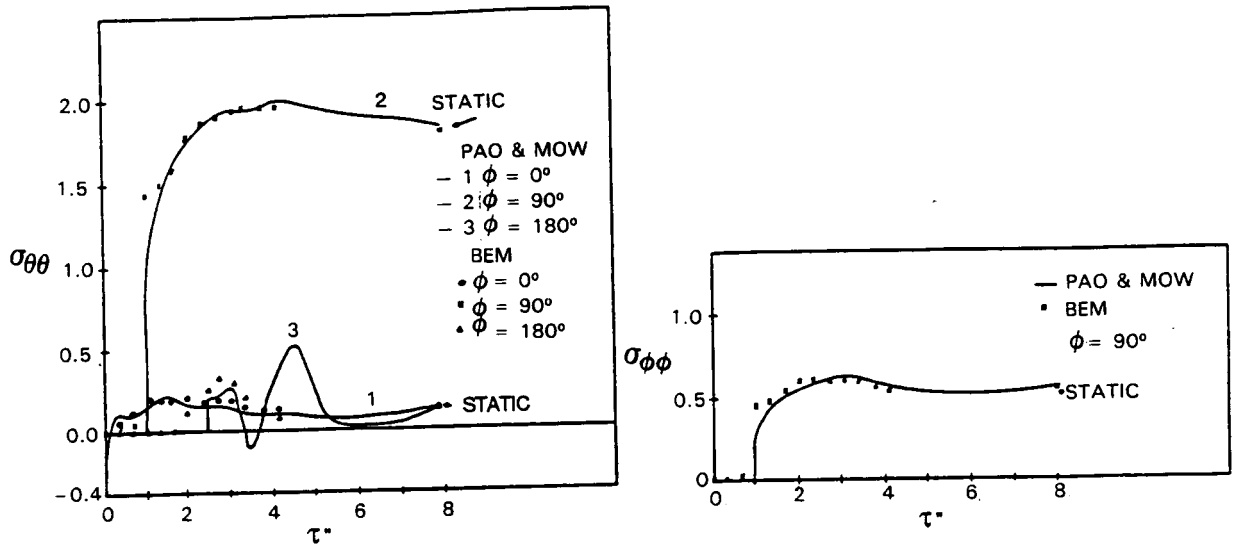

Figure 3.26: Hoop Stress Induced by Passage of Pressure Wave

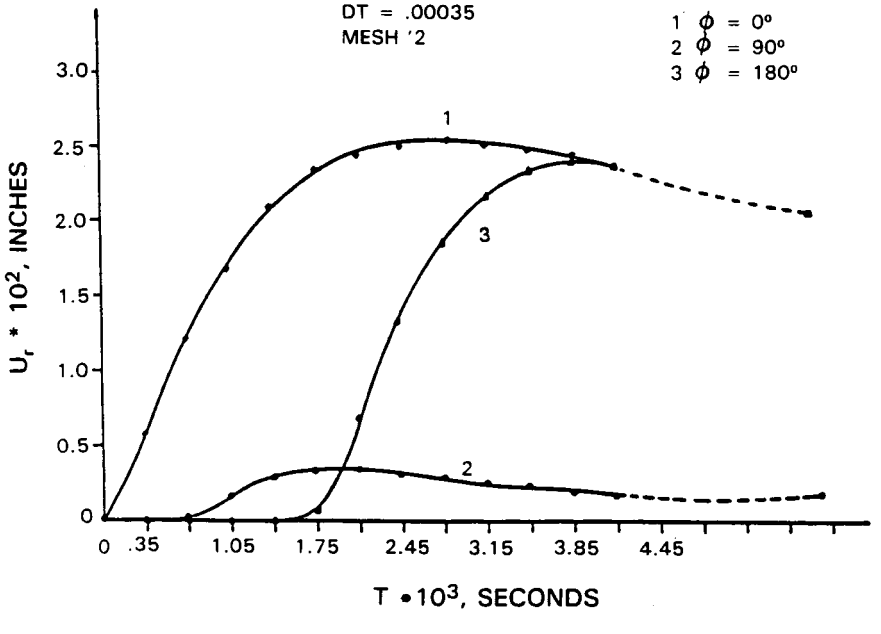

Figure 3.27: Radial Displacements Induced by Passage of Pressure Wave

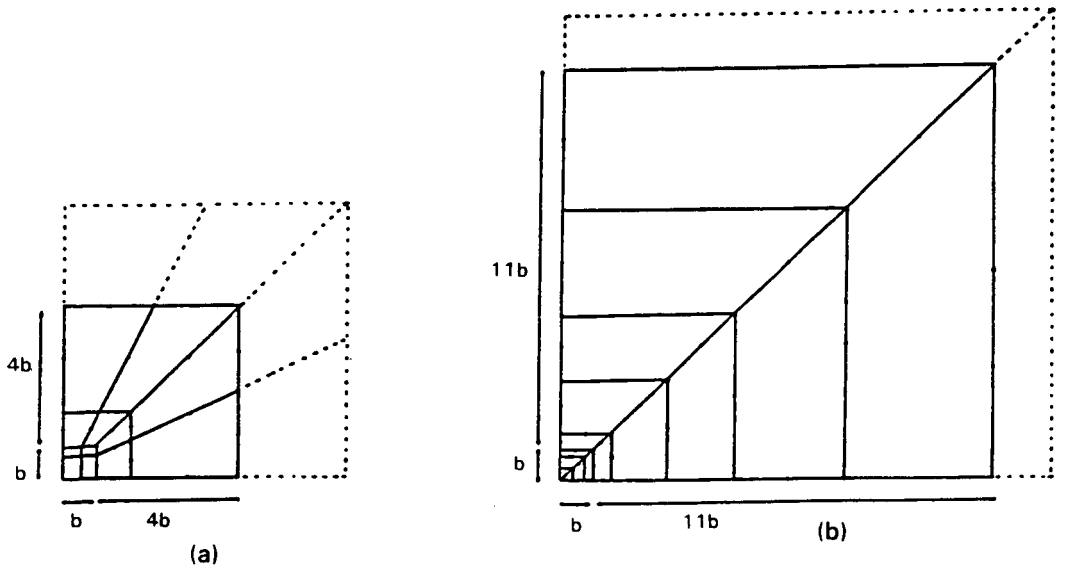

Figure 3.28: BEST3D Models for Analysis of Footing Compliance

The foundation is first subjected to a uniform harmonic vertical displacement u_z of amplitude equal to unity. The surface of the halfspace is traction free. The traction distribution under the foundation obtained by the boundary element method is integrated to give the total vertical load P_z. The normalized compliance of the foundation in the vertical direction is obtained as $C_{vv} = \mu b u_z / P_z$. T
modelling the foundation as well as surface of the halfspace. Since the transform domain computer program can take advantage of symmetry, only one-quarter of the problem needs to be discretized. The coarse mesh uses four and twelve elements to model the foundation and the halfspace, respectively. Note that the outermost four elements are infinite elements. This discretization results in 44 nodes. The finer mesh uses six and twelve elements for the same purpose, leading to two infinite elements and 65 nodes.

This problem was originally solved by Wong and Luco (1976). They numerically integrated the vertical displacement at the surface of a homogeneous halfspace due to a unit point load over the foundation, which was discretized into small squares. This problem was recently revisited by Rizzo, *et. al.* (1985) using a BEM approach. In their work both frictionless and welded cases are considered and two approaches are used: The exact one employs the halfspace kernels (Lamb's solution) and the approximate one uses the fullspace kernels (Stoke's solution). In both cases, only the rigid foundation is discretized and these two approaches are practically indistinguishable except at the very low frequency range. All three solutions mentioned are plotted in Fig. 3.29, along with the vertical compliance obtained by the present method, using the fine mesh. The good

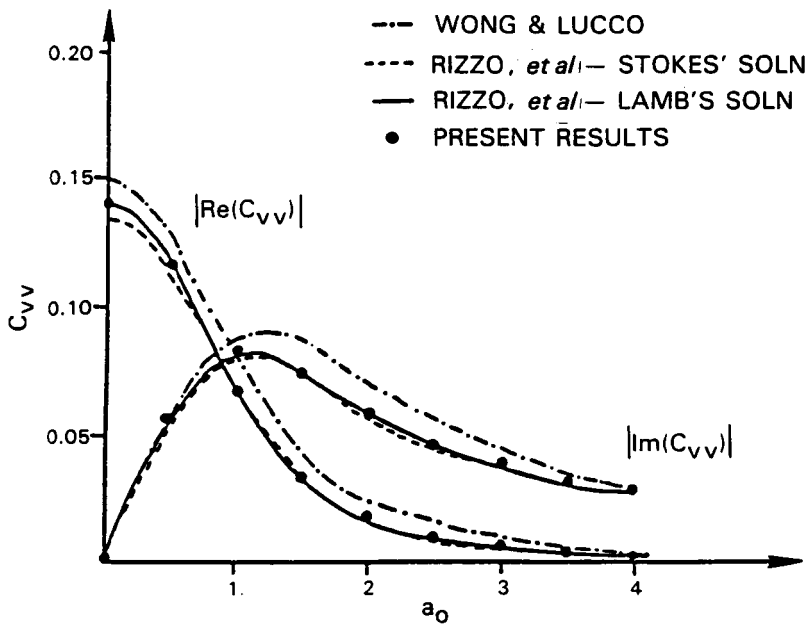

Figure 3.29: Vertical Compliance of Flexible Square Footing

agreement between the present results and that of Rizzo, *et. al.* (1985) should be noticed. The major difference between Wong and Luco's results and the boundary element results is due to the fact that quadratic shape functions are used for representation of the variation in the field variables over each element in the present work, as well as that of Rizzo, whereas Wong and Luco assumed that the unknown contact stresses are uniform within each element. Differences in the results from the coarse and fine meshes are quite small (Table 3.4).

Next the case of a transient loading was considered. The time step used for this analysis is $\Delta T = 0.2$. The time history of the applied pressure and the vertical displacements at the center and corner of the loaded area are plotted in Figure 3.30. It can be seen that the vertical displacement at the center of the footing converges to the static value after 2.4 seconds, whereas the vertical displacement at the corner of the footing converges to its static value at a later time. The mesh used for this problem gives a maximum error of 2% for static analysis. The results obtained for the present dynamic problem should have equivalent accuracy. This example shows the utility of the present algorithm for transient dynamic analysis of halfspace problems.

Table 3.4: Comparison of Vertical Compliances Obtained Using Two Different Meshes

	$\Re[C_{vv}(a_0)]$		$\Im[C_{vv}(a_0)]$	
$a_0 = \omega b/c_2$	Coarse Mesh	Fine Mesh	Coarse Mesh	Fine Mesh
0.5	.118	.117	-.057	-.058
1.0	.064	.069	-.083	-.081
1.5	.032	.034	-.076	-.070
2.0	.021	.018	-.059	-.052
2.5	.015	.015	-.052	-.048
3.0	.010	.012	-.036	-.037
3.5	.005	.006	-.035	-.032
4.0	.004	.004	-.027	-.027

3.5.8 NONLINEAR DYNAMIC RESPONSE OF A BAR

A bar with circular cross-section (of Section 3.5.5) is held along its sides by lubricated rollers and is fixed at one end. The free end is subjected to a suddenly applied and maintained uniform compression $t_z = -333$, which exceeds the yield stress of the bar (yield stress = 300). In this example, the bar has dimensions and material properties identical to that of the example discussed in Section 3.5.5. The discretization of the bar is similar to that shown in Figure 3.18 except that, in the present example, the full cross-section of the bar is modeled instead of one-quarter of it. The volume of the bar is discretized by using five equal twenty node volume cells. A bilinear stress-strain relation, as shown in Figure 3.31, is assumed. The time step used for this example is $\Delta T = 0.004473$. Use of a uniform time step is vital, as it allows reuse at each new time step of previously calculated matrices.

In Figure 3.31, the elasto-plastic response of the bar at time $T = 0.8T_e$ (where $T_e = c_1 T/L$, i.e. the time taken by the compression wave to reach the fixed end of the bar) is plotted against the one-dimensional analytical solution (Garnet and Armen, Ref. 32). The normal stress σ_{zz} is normalized by the elastic modulus and the distance along the bar is normalized by the length of the bar. The numerical results are in reasonable agreement with the analytical solution except for the sharp jumps in the stress which are diffused by the numerical analysis. The analytical solution of course can never match the real material response where it behaves more like the numerical solution. The major differences in the results between the two solutions can be attributed to the three-dimensional nature of the present example. As the bar is on lubricated rollers, in addition to longitudinal stress, lateral stresses also exist in the bar. Simple one-dimensional theory considers longitudinal stress only.

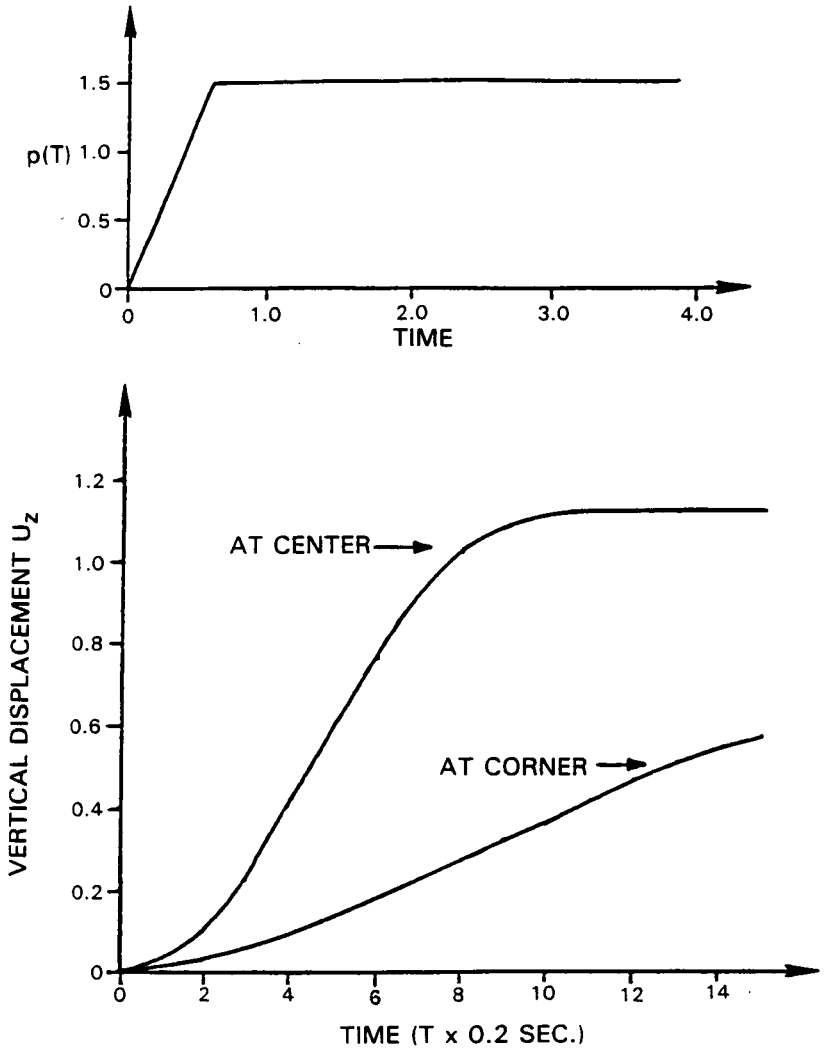

Figure 3.30: Transient Response of Flexible Square Footing

3.5.9 NATURAL FREQUENCIES OF A PARALLELEPIPED

Code validation and mesh sensitivity studies for the BEST3D natural frequency capability are being done using solutions obtained by Leissa and Zhang (Reference 33) for rectangular parallelpipeds. In the paper cited a Ritz technique is used to calculate the first five modes of each type (easy bending, stiff bending, torsion and extension) for a variety of geometries. Convergence studies in the paper indicate that the results for the first mode are accurate to better than 1%.

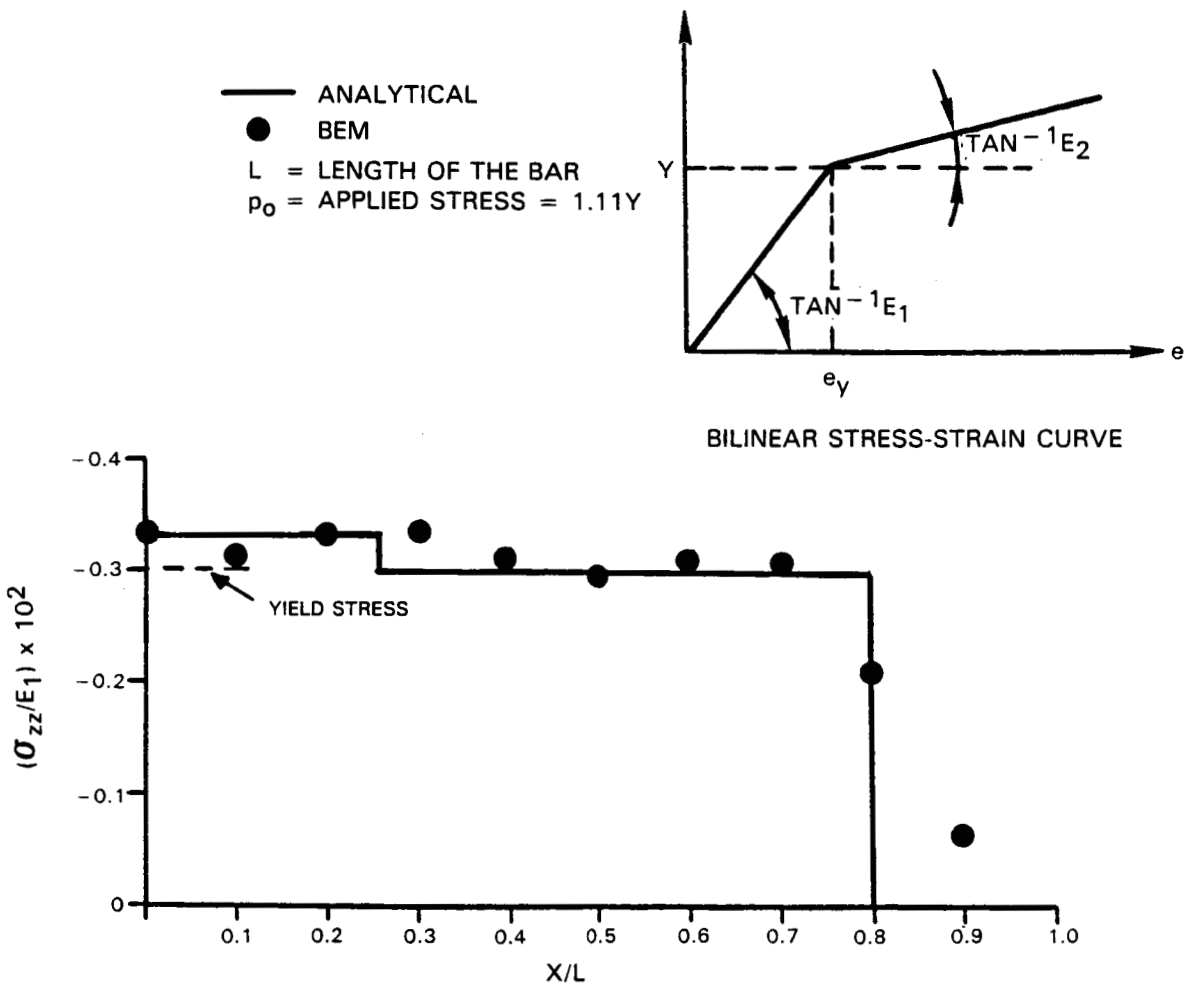

Figure 3.31: Transient Elasto-Plastic Response of a Bar Subjected to a Suddenly Applied and Maintained End Pressure

One of the cases studied is a parallelepiped (Figure 3.32) of dimensions 1 x 1 x 0.5, with one end completely fixed.

Four single region, quadratic BEST3D meshes (summarized in Table 3.5) were used in the study. The results of the study are shown in Table 3.6 for the first ten modes. Both the frequency parameter and the percentage deviation from the Ritz solution are given. It can be seen that rapid convergence is achieved for the first mode of each type by the addition of elements in the axial direction. Convergence of the higher modes, however, requires the use of additional elements in the chordwise direction as well.

It is planned to use the NASA twisted plate data (Reference 34) and associated analyt-

Table 3.5: BEST3D Models for $1 \times 1 \times 0.5$ Parallelepiped

Model	Elements			Total Elements	Source Points
	A	B	C		
1	1	1	1	6	20
2	1	2	1	10	32
3	1	3	1	14	44
4	2	3	1	22	68

Table 3.6: Convergence of BEST3D Natural Frequency Results

Mode	Type	Ritz	Mesh 1	(%)	Mesh 2	(%)	Mesh 3	(%)	Mesh 4	(%)
1	EB	0.447	0.472	5.5	0.429	-4.0	0.435	-2.7	0.442	-1.2
2	SB	0.667	0.664	-0.4	0.666	-0.3	0.668	0.1	0.661	-0.8
3	T	0.788	0.887	12.5	0.829	5.1	0.820	4.0	0.788	0.0
4	L	1.596	1.625	1.8	1.620	1.5	1.618	1.4	1.602	0.4
5	EB	1.664	2.136	28.3	1.797	8.0	1.729	3.9	1.689	1.5
6	SB	1.774			1.836	3.5	1.789	0.9	1.775	0.1
7	T	2.220			2.552	14.9	2.448	10.3	2.285	2.9
8	EB	2.278					3.033	33.3	2.365	3.8
9	L	2.797							2.842	1.6
10	SB	3.068							3.249	5.9

Mode Type Identification		Frequency Parameter $= w\sqrt{\rho/E}$
EB - Easy Bending SB - Stiff Bending T - Torsion L - Extension		

Table 3.7: Comparison of Ritz and BEST3D Results for Short, Thick Plate

Mode	Ritz	BEST3D	(%)
1 (easy bending)	3.38	3.20	-5.2
2 (torsion)	7.42	7.20	-2.8

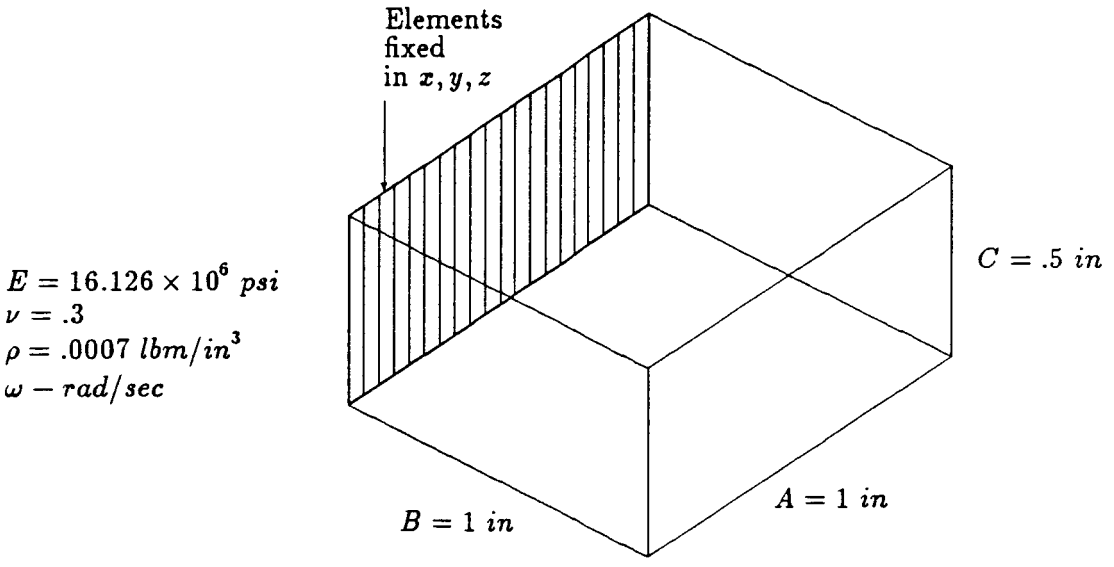

Figure 3.32: Geometry for Calibration of BEST3D Natural Frequency Analysis

ical results for the verification of the BEST3D natural frequency capability. The short, thick, untwisted plate (2 x 2 x .4) has already been analyzed using a model topologically equivalent to mesh 4 (above). The BEST3D results are compared, in Table 3.7, to results obtained using the Ritz method. The differences are somewhat larger than for the previous case. This is believed to be due primarily to the degeneration in the worst element aspect ratios, from 1.5 for the earlier case to 2.5 for the NASA plate. This assumption will be verified by using a somewhat refined, two-region model. Analysis of the twisted plate geometries will then be undertaken.

3.5.10 COMPONENT ANALYSIS

1. Directionally Solidified Turbine Blade

   In order to verify the utility of the exact kernel functions (described in Ref. 2) for component analysis, the high turbine blade (Figure 3.33) previously analyzed with isotropic material properties was reanalyzed with the properties of a directionally solidified aerospace alloy. As expected, this static analysis ran without difficulty, indicating that both the kernel function for hexagonal materials and the new particular solution for anisotropic centrifugal loads are operating correctly. The increase in cost relative to an isotropic analysis was approximately 30%.

2. Bearing Race

   A single pitch of a bearing inner race was analyzed to determine the stress near a drain hole connecting the axial groove to the channel in which the bearing travels.

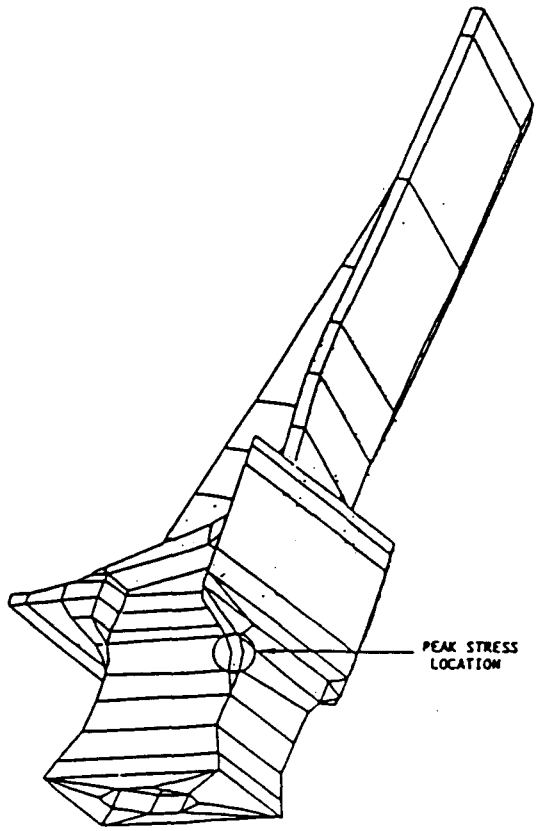

Figure 3.33: BEST3D Model of Anisotropic Turbine Blade

The main load involved are a preload on the inner diameter, centrifugal load and the roller load. It is of interest to determine the response for a variety of loading combinations, and, in particular, for various locations of the roller relative to the axial groove. The BEST3D model used for this analysis is shown in Figure 3.34. It consists of three subregions containing a total of 323 surface patches.

An initial analysis of the problem was carried out using linear variation of displacement and traction over all elements. As has been the case in previous complex analyses, the results were generally good but it was clear that improvement in accuracy was required in certain areas, particularly near the drain hole/groove intersection. To gain this improvement quadratic variation was used over 33 elements (10%). The increase in computing time was less than 25% and acceptable accuracy was achieved without the need to redefine the mesh. A typical contour plot of the hoop component of stress is shown in Figure 3.35.

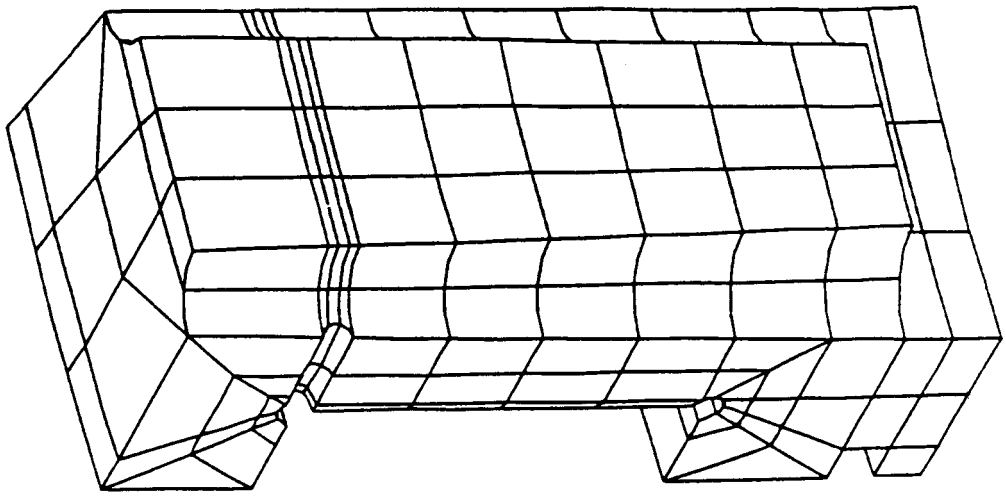

Figure 3.34: BEST3D Model of Single Pitch of Bearing Race

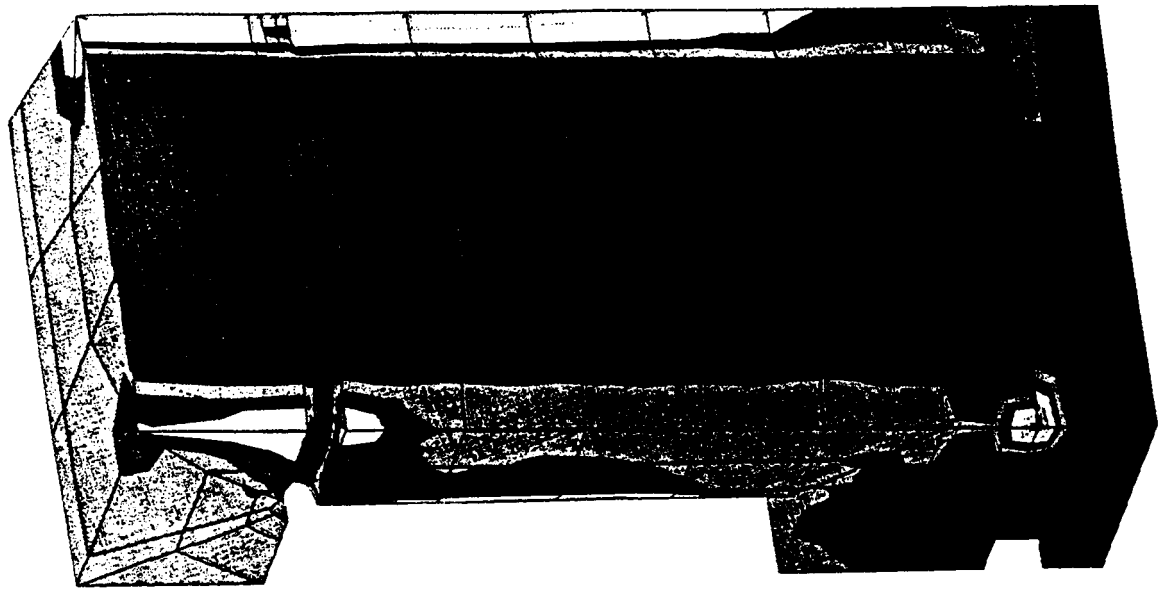

Figure 3.35: Hoop Stress Contours for Bearing Race

3.6 CONCLUSIONS

A number of significant conclusion can be drawn from the experience of the first three years of this program. While the issues involved have been discussed in some detail above, the are presented here in summary form.

1. The boundary element method is capable of producing accurate solutions to three-dimensional problems of plasticity, using a variety of algorithms.

2. Preliminary results indicate that natural frequencies can be successfully calculated using the three-dimensional boundary element method.

3. Elastodynamic analyses can be effectively treated using the boundary element method. While the nonlinear dynamic analysis has been formulated and implemented in preliminary form, a great deal of further work would be required to develop a usable tool for such problems.

4. Reduction in volume discretization is a key to the efficient use of the boundary element method. Exploitation of particular integrals should be pursued in order to eliminate or reduce the need for volume cell definitions.

5. Utilization of the special capabilities of supercomputers will be required for effective production use of three-dimensional boundary element analyses.

6. Existing pre- and post-processing systems can be easily modified to interface with BEST3D.

3.7 LIST OF SYMBOLS

δ_{ij}	Kronecker delta symbol
u_i, t_i	boundary displacements and tractions
G_{ij}	displacement point load solution
F_{ij}	traction kernel derived from G_{ij}
f_i	mechanical body forces
T	temperature
β	coefficient of thermal expansion
$B_{ijk}, T_{ijk}, D_{ijk}, S_{ijk}$	higher order kernels derived from G_{ij}
S	surface of three-dimensional structure
V	interior of a three-dimensional structure
σ_{ij}	stress tensor
ϵ_{ij}	strain tensor
c_{ij}	jump terms in boundary integral equation
$\dot{\lambda}$	plastic flow factor
$F(\sigma_{ij}, h)$	yield function
h	hardening parameter
$\cdot$, same as $\dot{\sigma}_{ij}$	time derivative
superscript ^{p}, as in ϵ^p_{ij}	plastic component
superscript ^{e}, as in ϵ^p_{ij}	elastic component
D^e_{ijkl}	elastic constitutive tensor
x, y, z	points in three-dimensional space
superscript $^\circ$, as in σ°_{ij}	initial stress (or strain)
B^σ_{ijkl}	higher order kernel derived from G_{ij}
$M^\beta(\eta)$	isoparametric shape functions for volume cells
$N^\alpha(\eta)$	isoparametric shape functions for shape patches
$\omega^a, \omega^b, \omega^c$	Gaussian quadrature weights
$\eta_{a,b,c}$	Gaussian quadrature points
C_{ijkl}	elastic constants for a general elastic material
N, A	6×6 matrices
λ, μ	Lamé constants
t, τ	denote time in dynamic analysis
$*$, as in $G_{ij} * t_i$	time convolution
M_1, M_2	shape functions for time variation
$[A^j_i], etc.$	coefficient matrices in time domain solution

3.8 REFERENCES

1. Todd, E. S., B. N. Cassenti, S. Nakazawa and P. K. Banerjee, *3-D Inelastic Analysis Methods for Hot Section Components - First Annual Status Report*, NASA CR-174700, United Technologies, Pratt & Whitney Engineering, East Hartford, CT.

2. Wilson, R. B., M. J. Bak, S. Nakazawa and P. K. Banerjee, *3-D Inelastic Analysis Methods for Hot Section Components - Second Annual Status Report*, NASA CR-175060, United Technologies, Pratt & Whitney Engineering, East Hartford, CT.

3. Dederichs, P. H. and G. Leibfried, "Elastic Green's Function for Anisotropic Cubic Crystals," *Physical Review*, 188, No. 3, 1969, pp 1175-1183.

4. Pan, Y.-C. and T.-W. Chou, "Point Force Solution for an Infinite Transversely Isotropic Solid," *JAM*, 43, 1976, pp 608-612.

5. Pan, Y.-C. and T.-W. Chou, "Green's Functions for Two-Phase Transversely Isotropic Materials," *JAM*, 46, 1979, pp 551-556.

6. Wilson, R.B. and T. A. Cruse, "Efficient Implementation of Anisotropic Three-dimensional Boundary Integral Equation Stress Analysis," *Int. J. Num. Meth. Eng.*, 12, 1978, pp 1383-1397.

7. Malen, K., "A Unified Six-Dimensional Treatment of Elastic Green's Functions and Dislocations," *Phys. Stat. Sol. (b)*, 44, 1971, pp 661-672.

8. Mukherjee, S., *Boundary Element Method in Creep and Fracture*, Applied Science Publishers, London,1983.

9. Fung, Y. C., *Foundations of Solid Mechanics*, Prentice-Hall, Inc., Englewood Cliffs, NJ, 1965.

10. Barr, D. T. and M. P. Cleary, "Elastostatic Interaction of Multiple Arbitrarily Shaped Cracks in Plane Inhomogeneous Regions," *Eng. Frac. Mech.*, 19, No. 3, 1984, pp 481-506.

11. Cleary, M. P., M. Kavvadas and K. Y. Lam, "Development of a Fully Three-Dimensional Simulator for Analysis and Design of Hydraulic Fracturing," MIT UFRAC Report No. REL-82-12,1982.

12. Annigeri, B. S. and M. P. Cleary, "Surface Integral Finite Element Hybrid (SIFEH) Method for Fracture Mechanics," *Int. J. Num. Meth. Eng.*, 20, 1984, pp 869-885.

13. Eshelby, J. D., "The Determination of the Elastic Field of an Ellipsoidal Inclusion and Related Problems," *Proc. Roy. Soc.*, A241, 1957, pp 376-396.

14. Banerjee, P. K. and R. Butterfield, *Boundary Element Methods in Engineering Science*, McGraw-Hill (UK), 1981.

15. Wilson, R. B., *BEST3D (Boundary Element Stress Technology - Three Dimensional)*, United Technologies, Pratt & Whitney Engineering, East Hartford, CT, 1985.

16. Saad, Y., "Chebyshev Acceleration Techniques for Solving Nonsymmetric Eigenvalue Problems," *Math. Comp.*, 42, No. 166, 1984, pp 567-588.

17. Dominquez, J., "Dynamic Stiffness of Rectangular Foundations," Report R78-20, Dept. of Civil Engineering, M.I.T.

18. Karabalis, D. L. and D. E. Bescos, "Dynamic Response of 3-D Rigid Foundations by Time Domain Boundary Element Method," *Earthquake Engineering and Structural Dynamics,* 12, 1984, pp 73-93.

19. Yoshida, K., T. Sato and H. Kawase, "Dynamic Response of Rigid Foundations Subjected to Various Types of Seismic Waves," Proceedings 8^{th} World Conference on Earthquake Engineering, California, 1984, pp 742-752.

20. Tanaka, Y. and T. Maeda, "Dynamic Interaction of Rigid Foundations Embedded in a Two-layer Visco-elastic Medium," Proceedings 8^{th} World Conference on Earthquake Engineering, California, 1984, pp 865-872.

21. Sen, R., T. G. Davies and P. K. Banerjee, "Dynamic Analysis of Pile Groups Embedded in Homogenous Soils," *International Journal of Earthquake Engineering and Structural Dynamics,* 13, 1985, pp 53-65.

22. Sen, R., E. Kausel and P. K. Banerjee, "Dynamic Analysis of Pile Groups Embedded in Non-homogenous Soils," *International Journal of Numerical and Analytical Methods in Geomechanics,* 9, 1985, pp 507-524.

23. Davies, T. G., R. Sen and P. K. Banerjee, "Pile Groups Embedded in Homogenous Soils," *Journal of Geotechnical Engineering Division,* A.S.C.E., December 1965.

24. Kaynia, A. and E. Kausel, "Dynamic Analysis of Piling Groups," Proceedings International Conference on Numerical methods in Offshore Piling, University of Texas at Austin, 1982.

25. Rizzo, F. J., D. J. Shippy and M. Rezayat, "Boundary Integral Analysis for a Class of Earth-structure Interaction Problems," Final report to NSF, Grant CEE80-13461, Department of Engineering Mechanics, University of Kentucky, 1985.

26. Kitahara, M. and K. Nakagawa, "Boundary Integral Equation Methods in Three-dimensional Elasto-dynamics," Proceedings 7^{th} International Conference on BEM, Lake Como, September 1985.

27. Hopkins, H. G., "Dynamic Expansion of Spherical Cavities in Metals," Chapter III in *Progress in Solid Mechanics*, 1, Edited by Sneddon, I. N., and R. Hill, North Holland, Amsterdam, 1963.

28. Hunter, S. C., Unpublished report, Ministry of Supply, United Kingdom, 1955, (cited in Reference 27).

29. Mikhlowicz, J., "The Theory of Elastic Waves and Wave Guides," *North Holland Series on Applied Mathematics and Mechanics*, 22, 1980.

30. Pao, Y. H. and C. C. Mow, *Diffraction of Elastic Waves and Dynamic Stress Concentration*, Crane Russak, N.Y., 1973.

31. Norwood, F. R. and J. Mikhlowicz, "Diffraction of Transient Elastic Waves by a Spherical Cavity," *Journal of Applied Mechanics*, 34, No. 3, 1967, pp 735-741.

32. Garnet, H. and H. Armen, "One Dimensional Elasto-plastic Wave Interaction and Boundary Reflections," *Computer and Structures*, 5, 1975, pp 327-334.

33. Leissa, A. and Z. Zhang, "On the Three-dimensional Vibrations of the Cantilevered Rectangular Parallelepiped," *J. Acoust. Soc. Am.* , 73 (6), June 1983, pp 2013-2021.

34. Kielb, R. E., A. W. Leissa, J. C. MacBain and K. S. Carney, "Joint Research Effort on Vibrations of Twisted Plates – Phase I: Final Results," NASA Reference Publication 1150, 1985.